Three dimensional analytical solution for finite circular cylinders subjected to indirect tensile test

X.X. Wei, K.T. Chau

PII: S0020-7683(13)00135-2
DOI: http://dx.doi.org/10.1016/j.ijsolstr.2013.03.026
Reference: SAS 7947

To appear in: *International Journal of Solids and Structures*

Received Date: 1 July 2011
Revised Date: 22 March 2013

Please cite this article as: Wei, X.X., Chau, K.T., Three dimensional analytical solution for finite circular cylinders subjected to indirect tensile test, *International Journal of Solids and Structures* (2013), doi: http://dx.doi.org/10.1016/j.ijsolstr.2013.03.026

Three dimensional analytical solution for finite circular cylinders subjected to indirect tensile test

X. X. Wei [a, b] and K. T. Chau [a*]

[a]*Department of Civil and Environmental Engineering, The Hong Kong Polytechnic University, Hung Hom, Kowloon, Hong Kong, China*

[b]*State Key Laboratory of Explosion Science and Technology, Department of Mechanics and Engineering, Beijing Institute of Technology, Beijing 100081，China*

(Submitted to *International Journal of Solids and Structures*)

ABSTRACT

This paper derives a new three-dimensional (3-D) analytical solution for the indirect tensile tests standardized by ISRM (International Society for Rock Mechanics) for testing rocks, and by ASTM (American Society for Testing and Materials) for testing concretes. The present solution for solid circular cylinders of finite length can be considered as a 3-D counterpart of the classical two dimensional (2-D) solutions by Hertz in 1883 and by Hondros in 1959. The contacts between the two steel diametral loading platens and the curved surfaces of a cylindrical specimen of length H and diameter D are modeled as circular-to-circular Hertz contact and straight-to-circular Hertz contact for ISRM and ASTM standards respectively. The equilibrium equations of the linear elastic circular cylinder of finite length are first uncoupled by using displacement functions, which are then expressed in infinite series of some combinations of Bessel functions, hyperbolic functions, and trigonometric functions. The applied tractions are expanded in Fourier-Bessel series and boundary conditions are used to yield a system of simultaneous equations. For typical rock cylinders of 54 mm diameter subjected to ISRM indirect tensile tests, the contact width is in the order of 2 mm (or a contact angle of 4 degrees) whereas for typical asphalt cylinders of 101.6 mm diameter subjected to ASTM indirect tensile tests the contact width is about 10mm (or a contact angle of 12 degrees). For such contact conditions, 50 terms in both Fourier and Fourier-Bessel series expansions are found sufficient in yielding converged solutions. The maximum hoop stress is always observed within the central portion on a circular section close to the flat end surfaces. The difference in the maximum hoop stress between the 2-D Hondros solution and the present 3-D solution increases with the aspect ratio H/D as well as Poisson's ratio ν. When contact friction is neglected, the effect of loading platen stiffness on tensile stress in cylinders is found negligible. For the aspect ratio of H/D = 0.5 recommended by ISRM and ASTM, the error in tensile strength may be up to 15% for both typical rocks and asphalts, whereas for longer cylinders with H/D up to 2 the error ranges from 15% for highly

compressible materials, and to 60% for nearly incompressible materials. The difference in compressive radial stress between the 2-D Hertz solution or 2-D Hondros solution and the present 3-D solution also increases with Poisson's ratio and aspect ratio *H/D*. In summary, the 2-D solution, in general, underestimates the maximum tensile stress and cannot predict the location of the maximum hoop stress which typically locates close to the end surfaces of the cylinder.

Keywords: Analytical solution; indirect tensile test; Brazilian test; asphalt; rocks; concretes

1. Introduction

One distinct mechanical characteristic of brittle materials is that they are strong in compression but much weaker in tension. Therefore, tensile strength is a very important index in describing brittle materials because it is more relevant to the mechanical failure of brittle solids than compressive strength. However, direct tensile test is very difficult to apply to brittle materials without inducing any eccentric moment. Therefore, various types of indirect tensile tests have been developed in order to measure the tensile strength of brittle materials, including the diametral compression on disk with central hole (Hobbs, 1965), the point load strength test (Wei et al., 1999; Chau and Wei, 2001; Wei and Chau, 2002), the double-punch test (Wei and Chau, 2000), and the diametral compression on the curved surface of cylindrical specimens (ISRM, 1978; ASTM, 2004).

The most popular indirect tensile strength test for testing rocks and concretes is the so-called Brazilian test (Fig. 1(a)), which was independently proposed by Akazawa in 1943 as a PhD thesis (Machida, 1975; Akazawa, 1953; Fairbairn and Ulm, 2002) and by Carneiro in 1943 at the Fifth Meeting at of the Brazilian Association for Technical Rules Standardization (Carneiro, 1943; Carneiro and Barcellos, 1953; Fairbairn and Ulm, 2002). The testing procedure for indirect tensile test was standardized by International Society for Rock Mechanics (Bieniawski and Hawkes, 1978; ISRM, 1978), while the most commonly used indirect tensile test for concrete was standardized by American Society for Testing and

Materials (ASTM, 2004). As shown in Fig. 1, finite circular solid cylinders of length H and diameter D are used for both the ISRM indirect tensile test and the ASTM indirect tensile. Although two diametral strips of loading are adopted for both ISRM and ASTM tests, the loading platens are of different shapes. The recommended height-to-diameter ratios (H/D) for both ISRM (1978) and ASTM (2004) standards are 0.5. Note that the old standard of ASTM (1995) for bituminous material recommended H/D = 0.625 but it was withdrawn in 2003. The failure mode of cylindrical specimens under both ISRM and ASTM tests is always in brittle splitting along the plane formed by joining the two loading strips, as illustrated by the vertical lines shown in Fig.1. Indirect tensile test is sometimes referred as the "splitting test" (Rocco et al., 1999; Rocco et al., 2001). In this paper, the stress distribution for both contact conditions proposed by ISRM and ASTM shown in Fig. 1(a) and Fig. 1(c) will be considered.

An analytical solution for a solid circular cylinder subjected to two concentrated diametral line loads was derived by Hertz in 1883 (p. 124, Timoshenko and Goodier, 1982). The main feature of this solution is that a uniform tensile stress is predicted on the vertical plane formed by joining the two line loads. This uniform tensile stress is found equal to $2F_1/(\pi DH)$, where F_1 is the total applied force and D and H are the diameter and length of the cylinder respectively. Indeed, circular cylinders did fail in tension between these two line loads in all brittle materials (see Fig. 1). Not surprisingly, this simple and elegant solution has been adopted in the standard testing procedures proposed by both ISRM and ASTM. Hondros (1959) extended the solution to the case of applied load being modeled as uniformly distributed strip loads. The 2-D stress components by Hondros (1959) are summarized in Eqs. (5) and (6) of Section 10.7 of Jaeger and Cook (1976) and reproduced here in Appendix B for the sake of completeness. Both of these two-dimensional (2-D) solutions are valid for either very long cylinders (plane strain condition) or very short cylinders (plane stress condition). However, the suggested H/D value in both ISRM and ASTM standards is 0.5 (ISRM, 1978;

ASTM, 2004). It seems that this value may not fully justify the use of the 2-D solution. Indeed, it is more often found that the experimental results cannot be well described by the 2-D analytical solution (Chen and Chen, 1976; Mamlouk et al., 1983; Rocco et al., 2001; Yu et al., 2006).

Therefore, finite element method (FEM) has been employed to study the stress distribution within finite circular cylinders under the indirect tensile test. For example, Yu et al. (2006) studied the shape effect in the Brazilian test using 3D FEM. Numerical results show that for a fixed Poisson's ratio of 0.22 the tensile stress distribution along both the compressed diameter and thickness is not uniform, and the tensile stress near the end surface of the specimen is higher than that of the inner part. It was also found that the 2-D solution by Hertz in 1883 and by Hondros (1959) is not accurate enough to calculate the tensile strength of rocks, especially for relatively thick cylinders. Roque and Buttlar (1992) applied FEM to analyze the indirect tensile test for asphalts and demonstrated that there is a significant variation of the tensile stress along the thickness of the cylinder. Moreover, the two dimensional solutions by Hertz in 1883 and by Hondros (1959) also fail to consider the Poisson effect.

The main objective of this study is to obtain a three-dimensional (3-D) analytical solution for the indirect tensile test, and through this new solution to investigate the validity of 2-D solution in applying to indirect tensile tests. The method of solutions follows the displacement function approach (Muki, 1960; Chau and Wei, 2000, 2001) in converting the coupled equilibrium equations for displacements to a system of two uncoupled differential equations of biharmonic equation and Laplace equation. In cylindrical coordinate, the general solutions of these two displacement functions are expressed in terms of series solution consisting of Bessel functions, hyperbolic functions, and trigonometric functions. In fact, the most difficult step in the solution technique is to assume an appropriate form of solution such that all

boundary conditions can be satisfied exactly. In order to satisfy the boundary conditions, Fourier-Bessel expansion technique is applied to expand the applied traction on the curved surface.

The present solution provides a theoretical basis for the stress analysis of and strength interpretation for the commonly adopted indirect tensile strength tests. In view of the popularity of the indirect tensile test in applying to various engineering materials, such as concrete, rocks and asphalts, the present solution is of fundamental importance to the area of material testing. The present 3-D solution also provides a major improvement over the 2-D solution of Hertz in 1883 (Timoshenko and Goodier, 1982) and Hondros (1959), and can be used to examine the effect of Poisson's ratio and shape effect of the specimen on the stress distribution within finite circular cylinders subjected to the indirect tensile test.

2. Mathematical Formulation

Figure 1 shows the typical experimental setup for the ISRM indirect tensile test (Fig. 1(a)) and the ASTM indirect tensile test (Fig. 1(c)). We assume that external loads are applied on a cylindrical specimen by two metal loading platens, one on the top and one at the bottom. For the ISRM test, the steel loading platens are in concave circular shape, whereas for the ASTM indirect tensile test, the steel loading platens are flat. For both the ISRM and ASTM indirect tensile tests, the external load is modeled by non-uniform radial Hertz contact stress as shown in Fig. 1(b). The cylinder is of radius R (or diameter $D = 2R$) and length $H = 2h$, and is assumed homogeneous, linear elastic and isotropic. The origin and the z-axis of the cylindrical coordinate (r, θ, z) coincide with the center and the axis of symmetry of the cylinder.

The traction free end boundary conditions for a finite solid circular cylinder under the indirect tensile test can be written as

$$\sigma_{zz} = 0, \quad \sigma_{zr} = 0, \quad \sigma_{z\theta} = 0 \tag{1}$$

on $z = \pm h$; and the strip loading on the curved boundary are modeled by Hertz contact as (see section 141 of Timoshenko and Goodier, 1982):

$$\sigma_{r\theta} = 0 \tag{2}$$

$$\sigma_{rz} = 0 \tag{3}$$

$$\sigma_{rr} = \begin{cases} -\dfrac{2F}{\pi b}\left(1-\dfrac{R^2\theta^2}{b^2}\right)^{1/2} & \text{for} \quad |\theta| \le \dfrac{b}{R} \quad \text{and} \quad |\pi-\theta| \le \dfrac{b}{R} \\ 0 & \text{for} \quad |\theta| > \dfrac{b}{R} \quad \text{and} \quad |\pi-\theta| > \dfrac{b}{R} \end{cases} \tag{4}$$

on $r = R$, where $\pi \approx 3.141592654$, θ is defined in Fig. 1(b) and measured in radian, F is the total force per unit length induced by the loading strips, and b is the half-width of the loading strips (see Fig. 1b). Note that this radial stress is zero at the edge of the contact zone (i.e. $R\theta = b$) and attains a maximum at the center of the contact width (i.e. $\theta = 0$). The contact width can be determined as (Timoshenko and Goodier, 1982)

$$b = \sqrt{\frac{4FR_1R}{\pi(R_1+R)}\left\{\frac{1-\nu^2}{E}+\frac{1-\bar{\nu}^2}{\bar{E}}\right\}} \tag{5}$$

where R_1 is the radius of the loading platens, E is the Young's modulus and ν is the Poisson's ratio of the cylinder; whereas the elastic properties of the loading platens are denoted by the superimposed bar. For the ISRM (1978) indirect tensile test shown in Fig. 1(a), the concave contact has a radius of $R_1 = -1.5R$; whereas for the ASTM (2004) indirect tensile test shown in Fig. 1(c), the flat platen has a radius of $R_1 \to \infty$. Thus, the platen contact width depends on the applied force F, the elastic properties (E and ν) of the cylinder, the radius of the cylinder R and the testing set-up of the loading platens (i.e. the value of R_1), as well as the elastic properties of the loading platens ($\bar{E}$ and $\bar{\nu}$).

3. Displacement Functions

In this study, the displacement function approach is employed to investigate analytically the 3-D stress distribution of cylinders subjected to the indirect tensile test. This method was originally proposed by Muki (1960) and has been discussed in details by Chau and Wei (2000, 2001) and by Chau (2013). These displacement functions consist of the *z*-component of the Galerkin vector plus the *z*-component of the irrotational part of the Helmholtz decomposition vector (see Section 4.9.1 of Chau, 2013). In particular, two displacement functions Φ (*z*-component of the Galerkin vector) and Ψ (*z*-component of the irrotational part of the Helmholtz decomposition vector) are introduced to uncouple the equilibrium equations leading to the following biharmonic and Laplace equations (Muki, 1960; Little, 1973; Chau, 2013)

$$\nabla^4\Phi = \nabla^2\nabla^2\Phi = 0, \quad \nabla^2\Psi = 0 \tag{6}$$

where ∇^2 is the Laplacian operator. In cylindrical coordinates, all displacement components (u_r, u_θ, u_z) and stress components (σ_{rr}, σ_{zz}, $\sigma_{\theta\theta}$, σ_{rz}, $\sigma_{r\theta}$, $\sigma_{z\theta}$) can now be expressed in terms of these two displacement functions Φ and Ψ as

$$u_r = \frac{\partial^2\Phi}{\partial r\partial z} + \frac{1}{r}\frac{\partial\Psi}{\partial\theta}, \quad u_\theta = \frac{1}{r}\frac{\partial^2\Phi}{\partial\theta\partial z} - \frac{\partial\Psi}{\partial r}, \quad u_z = -[2(1-\nu)\nabla_1\Phi + (1-2\nu)\frac{\partial^2\Phi}{\partial z^2}] \tag{7}$$

$$\sigma_{rr} = -2\nu G\nabla^2\frac{\partial\Phi}{\partial z} + 2G[\frac{\partial^3\Phi}{\partial z\partial r^2} + \frac{\partial}{\partial r}(\frac{1}{r}\frac{\partial\Psi}{\partial\theta})] \tag{8}$$

$$\sigma_{\theta\theta} = -2\nu G\nabla^2\frac{\partial\Phi}{\partial z} + 2G[\frac{1}{r}\frac{\partial^2\Phi}{\partial z\partial r} + \frac{1}{r^2}\frac{\partial^3\Phi}{\partial\theta^2\partial z} - \frac{\partial}{\partial r}(\frac{1}{r}\frac{\partial\Psi}{\partial\theta})] \tag{9}$$

$$\sigma_{zz} = -2G[(2-\nu)\frac{\partial}{\partial z}\nabla^2 - \frac{\partial^3}{\partial z^3}]\Phi \tag{10}$$

$$\sigma_{rz} = 2G[-(1-\nu)\frac{\partial}{\partial r}\nabla_1 + \nu\frac{\partial^3}{\partial r\partial z^2}]\Phi + \frac{G}{r}\frac{\partial^2\Psi}{\partial\theta\partial z} \tag{11}$$

$$\sigma_{z\theta} = 2G[-(1-\nu)\frac{1}{r}\frac{\partial}{\partial\theta}\nabla_1 + \nu\frac{1}{r}\frac{\partial^3}{\partial\theta\partial z^2}]\Phi - G\frac{\partial^2\Psi}{\partial r\partial z} \tag{12}$$

$$\sigma_{r\theta} = 2G[\frac{\partial}{\partial r}(\frac{1}{r}\frac{\partial^2 \Phi}{\partial \theta \partial z}) + \frac{1}{2}(\frac{1}{r}\frac{\partial \Psi}{\partial r} + \frac{1}{r^2}\frac{\partial^2 \Psi}{\partial \theta^2} - \frac{\partial^2 \Psi}{\partial r^2})] \tag{13}$$

where G and ν are the shear modulus and Poisson's ratio, respectively, and ∇^2 and ∇_1 are defined as

$$\nabla^2 = \frac{1}{r}\frac{\partial}{\partial r}(r\frac{\partial}{\partial r}) + \frac{1}{r^2}\frac{\partial^2}{\partial \theta^2} + \frac{\partial^2}{\partial z^2} = \nabla_1 + \frac{\partial^2}{\partial z^2} \tag{14}$$

The most crucial step in the method of solutions is to select appropriate forms of Φ and Ψ such that both Eq. (6) and the boundary conditions expressed by Eqs. (1-4) are satisfied. By specializing the series expressions for Φ and Ψ proposed by Chau and Wei (2000, 2001), the following solution forms are used:

$$\begin{aligned}\Phi = -A_0\frac{z^3}{12G} - C_0\frac{z}{4G}r^2 - \frac{1}{2G}\sum_{n=0}^{\infty}\Bigg\{ & H_{0n}r^{2n+2}z + \sum_{m=1}^{\infty}\frac{1}{\eta_m^3}[A_{mn}r\frac{\partial I_{2n}(\eta_m r)}{\partial r} + B_{mn}I_{2n}(\eta_m r)]\sin(\eta_m z) \\ & + \sum_{s=1}^{\infty}\frac{1}{\gamma_s^3}[C_{sn}\sinh(\gamma_s z) + D_{sn}\gamma_s z\cosh(\gamma_s z)]J_{2n}(\gamma_s r)\Bigg\}\cos(2n\theta)\end{aligned} \tag{15}$$

$$\Psi = -\frac{1}{2G}\sum_{n=0}^{\infty}\left\{E_{0n}r^{2n} + \sum_{m=1}^{\infty}\frac{E_{mn}}{\eta_m^2}I_{2n}(\eta_m r)\cos(\eta_m z) + \sum_{s=1}^{\infty}\frac{F_{sn}}{\gamma_s^2}\cosh(\gamma_s z)J_{2n}(\gamma_s r)\right\}\sin(2n\theta) \tag{16}$$

where $\eta_m = m\pi/h$, $\gamma_s = \lambda_s/R$, and λ_s is the s-th root of $J'_{2n}(\lambda_s) = 0$ (i.e. the derivative of the Bessel function of the first kind of order $2n$); $J_{2n}(x)$ and $I_{2n}(x)$ are the Bessel and modified Bessel functions of the first kind of order $2n$, respectively (Abramowitz and Stegun, 1965); and A_0, C_0, H_{0n}, E_{0n}, $A_{mn}, B_{mn}, C_{sn}, D_{sn}$, E_{mn} and F_{sn} are unknown coefficients to be determined by the boundary conditions.

In obtaining Eqs. (15) and (16), we note that the first term in Ψ given in Eq. (23) of Chau and Wei (2000) is not needed as there is no constant shear stress applied on the cylinders. In addition, the periodicity of the problem is now π with respect to the top and bottom loading platens on the cylinder as shown Fig. 1. That is, we have $\omega_n = 2n\pi/\pi = 2n$ in Eqs. (23-24) of Chau and Wei (2000). As θ is measured from the vertical and thus symmetry in the radial

displacement requires that it is a function of $\cos\theta$ only, but not function of $\sin\theta$ because sine function is antisymmetric. Therefore, it is necessary and sufficient to take the upper θ-dependence functions given in Eqs. (23-24) of Chau and Wei (2000). Similarly, because of the traction free conditions at the flat end boundaries of the cylinder, we can take the upper z-dependent functions of cosine and hyperbolic cosine in Eq. (23) of Chau and Wei (2000) for Ψ, and take the upper z-dependent functions of hyperbolic sine and hyperbolic cosine in Eq. (24) of Chau and Wei (2000) for Φ.

It is straightforward to show that the mathematical forms of Φ and Ψ given in Eqs. (15-16) satisfy Eq. (6) identically. Substitution of Eqs. (15-16) into Eqs. (8-13) yields the following expressions for the stress components

$$\begin{aligned}
\sigma_{rr} &= (2\nu-1)C_0 + \nu A_0 + \sum_{n=0}^{\infty}\Big\{ -2n(2n-1)E_{0n}r^{2n-2} + H_{0n}[\nu(8n+4)-(4n^2+6n+2)]r^{2n} \\
&+ \sum_{m=1}^{\infty}\Big\{ A_{mn}[2\nu I_{2n}(\eta_m r) - \frac{1}{\eta_m^2}\frac{\partial^2}{\partial r^2}(r\frac{\partial I_{2n}(\eta_m r)}{\partial r})] - \frac{B_{mn}}{\eta_m^2}\frac{\partial^2 I_{2n}(\eta_m r)}{\partial r^2} \\
&- \frac{2nE_{mn}}{\eta_m^2}\frac{\partial}{\partial r}(\frac{I_{2n}(\eta_m r)}{r})\Big\}\cos(\eta_m z) + \sum_{s=1}^{\infty}\Big\{ -\frac{2nF_{sn}}{\gamma_s^2}\frac{\partial}{\partial r}(\frac{J_{2n}(\gamma_s r)}{r})\cosh(\gamma_s z) \\
&+ [(C_{sn}+(2\nu+1)D_{sn})\cosh(\gamma_s z) + D_{sn}\gamma_s z\sinh(\gamma_s z)]J_{2n}(\gamma_s r) \\
&+ [(C_{sn}+D_{sn})\cosh(\gamma_s z) + D_{sn}\gamma_s z\sinh(\gamma_s z)][\frac{1}{\gamma_s^2 r}\frac{\partial J_{2n}(\gamma_s r)}{\partial r} - \frac{4n^2}{\gamma_s^2 r^2}J_{2n}(\gamma_s r)]\Big\}\Big\}\cos(2n\theta)
\end{aligned} \tag{17}$$

$$\begin{aligned}
\sigma_{\theta\theta} &= (2\nu-1)C_0 + \nu A_0 + \sum_{n=0}^{\infty}\Big\{ 2n(2n-1)E_{0n}r^{2n-2} + H_{0n}[\nu(8n+4)+(4n^2-2n-2)]r^{2n} \\
&+ \sum_{m=1}^{\infty}\Big\{ A_{mn}[2\nu I_{2n}(\eta_m r) - \frac{1}{\eta_m^2}\frac{1}{r}\frac{\partial}{\partial r}(r\frac{\partial I_{2n}(\eta_m r)}{\partial r}) + \frac{4n^2}{\eta_m^2 r}\frac{\partial I_{2n}(\eta_m r)}{\partial r}] \\
&- \frac{B_{mn}}{\eta_m^2}[\frac{1}{r}\frac{\partial I_{2n}(\eta_m r)}{\partial r} - \frac{4n^2}{r^2}I_{2n}(\eta_m r)] + \frac{2nE_{mn}}{\eta_m^2}\frac{\partial}{\partial r}(\frac{I_{2n}(\eta_m r)}{r})\Big\}\cos(\eta_m z) \\
&+ \sum_{s=1}^{\infty}\Big\{ 2\nu D_{sn}\cosh(\gamma_s z)J_{2n}(\gamma_s r) - [(C_{sn}+D_{sn})\cosh(\gamma_s z) + D_{sn}\gamma_s z\sinh(\gamma_s z)] \\
&\times [\frac{1}{\gamma_s^2 r}\frac{\partial J_{2n}(\gamma_s r)}{\partial r} - \frac{4n^2}{\gamma_s^2 r^2}J_{2n}(\gamma_s r)] + \frac{2nF_{sn}}{\gamma_s^2}\frac{\partial}{\partial r}(\frac{J_{2n}(\gamma_s r)}{r})\cosh(\gamma_s z)\Big\}\Big\}\cos(2n\theta)
\end{aligned} \tag{18}$$

$$\sigma_{zz}=2(2-\nu)C_0+(1-\nu)A_0+\sum_{n=0}^{\infty}\Big\{\ H_{0n}(2-\nu)(8n+4)r^{2n}+\sum_{m=1}^{\infty}\Big\{\ A_{mn}[2(2-\nu)I_{2n}(\eta_m r)$$
$$+r\frac{\partial I_{2n}(\eta_m r)}{\partial r}]+B_{mn}I_{2n}(\eta_m r)\ \Big\}\cos(\eta_m z) \tag{19}$$
$$-\sum_{s=1}^{\infty}\Big\{\ [C_{sn}+(2\nu-1)D_{sn}]\cosh(\gamma_s z)+D_{sn}\gamma_s z\sinh(\gamma_s z)\ \Big\}J_{2n}(\gamma_s r)\Big\}\cos(2n\theta)$$

$$\sigma_{rz}=\sum_{n=0}^{\infty}\Big\{\ 2n(8n+4)(1-\nu)H_{0n}r^{2n-1}z+\sum_{m=1}^{\infty}\Big\{-\frac{A_{mn}}{\eta_m}[2(\nu-1)\frac{\partial I_{2n}(\eta_m r)}{\partial r}-\frac{\partial}{\partial r}(r\frac{\partial I_{2n}(\eta_m r)}{\partial r})]$$
$$+\frac{B_{mn}}{\eta_m}\frac{\partial I_{2n}(\eta_m r)}{\partial r}+\frac{nE_{mn}}{\eta_m}\frac{I_{2n}(\eta_m r)}{r}\Big\}\sin(\eta_m z)+\sum_{s=1}^{\infty}\Big\{-\frac{nF_{sn}}{\gamma_s}\frac{J_{2n}(\gamma_s r)}{r}\sinh(\gamma_s z) \tag{20}$$
$$-\frac{1}{\gamma_s}[(C_{sn}+2\nu D_{sn})\sinh(\gamma_s z)+D_{sn}\gamma_s z\cosh(\gamma_s z)]\frac{\partial J_{2n}(\gamma_s r)}{\partial r}\Big\}\Big\}\cos(2n\theta)$$

$$\sigma_{z\theta}=\sum_{n=0}^{\infty}\Big\{-2n(8n+4)(1-\nu)H_{0n}r^{2n-1}z+\sum_{m=1}^{\infty}\Big\{\frac{2nA_{mn}}{\eta_m}[2(\nu-1)\frac{I_{2n}(\eta_m r)}{r}-\frac{\partial I_{2n}(\eta_m r)}{\partial r}]$$
$$-\frac{2nB_{mn}}{\eta_m}\frac{I_{2n}(\eta_m r)}{r}-\frac{E_{mn}}{2\eta_m}\frac{\partial I_{2n}(\eta_m r)}{\partial r}\Big\}\sin(\eta_m z)+\sum_{s=1}^{\infty}\Big\{\frac{F_{sn}}{2\gamma_s}\frac{\partial J_{2n}(\gamma_s r)}{\partial r}\sinh(\gamma_s z) \tag{21}$$
$$+\frac{2n}{\gamma_s}[(C_{sn}+2\nu D_{sn})\sinh(\gamma_s z)+D_{sn}\gamma_s z\cosh(\gamma_s z)]\frac{J_{2n}(\gamma_s r)}{r}\Big\}\Big\}\sin(2n\theta)$$

$$\sigma_{r\theta}=\sum_{n=0}^{\infty}\Big\{2n(2n-1)E_{0n}r^{2n-2}+2n(2n+1)H_{0n}r^{2n}+\sum_{m=1}^{\infty}\Big\{\frac{2nA_{mn}}{\eta_m^2}\frac{\partial^2 I_{2n}(\eta_m r)}{\partial r^2}+\frac{2nB_{mn}}{\eta_m^2}$$
$$\times[\frac{1}{r}\frac{\partial I_{2n}(\eta_m r)}{\partial r}-\frac{1}{r^2}I_{2n}(\eta_m r)]+\frac{E_{mn}}{2\eta_m^2}[-\frac{1}{r}\frac{\partial I_{2n}(\eta_m r)}{\partial r}+\frac{4n^2}{r^2}I_{2n}(\eta_m r)+\frac{\partial^2 I_{2n}(\eta_m r)}{\partial r^2}]\Big\}\cos(\eta_m z) \tag{22}$$
$$+\sum_{s=1}^{\infty}\frac{2n}{\gamma_s^2}[(C_{sn}+D_{sn})\cosh(\gamma_s z)+D_{sn}\gamma_s z\sinh(\gamma_s z)][\frac{1}{r}\frac{\partial J_{2n}(\gamma_s r)}{\partial r}-\frac{1}{r^2}J_{2n}(\gamma_s r)]$$
$$-\sum_{s=1}^{\infty}\frac{F_{sn}}{\gamma_s^2}[\frac{1}{r}\frac{\partial J_{2n}(\gamma_s r)}{\partial r}+(\frac{\gamma_s^2}{2}-\frac{4n^2}{r^2})J_{2n}(\gamma_s r)]\cosh(\gamma_s z)\Big\}\sin(2n\theta)$$

The resilient modulus is very useful for the evaluation of the quality of the bituminous materials and pavement design (Croney and Croney, 1998). Because the resilient modulus is usually obtained in experiments by measuring the displacement component u_z on the end surfaces of the cylinder during the so called “Marshall test” which is essential an indirect test for bituminous material (Roque and Buttlar, 1992; Webb et al., 1985), the expression of the

displacement component u_z is also given here. In particular, substitution of Eqs. (15-16) into the third of Eq. (7) yields the following expression for displacement component u_z as

$$u_z = \frac{1}{2G}\Bigg\{[(1-2\nu)A_0 + 4(1-\nu)C_0]z + \sum_{n=0}^{\infty}\Bigg\{ H_{0n}(8n+4)(2-2\nu)r^{2n}z + \sum_{m=1}^{\infty}\Bigg\{\frac{A_{mn}}{\eta_m}[4(1-\nu)I_{2n}(\eta_m r) + r\frac{\partial I_{2n}(\eta_m r)}{\partial r}] + \frac{B_{mn}}{\eta_m} I_{2n}(\eta_m r)\Bigg\}\sin(\eta_m z) - \sum_{s=1}^{\infty} J_{2n}(\gamma_s r)\Bigg\{\frac{C_{sn}}{\gamma_s}\sinh(\gamma_s z) + \frac{D_{sn}}{\gamma_s}[-2(1-2\nu)\sinh(\gamma_s z) + \gamma_s z\cosh(\gamma_s z)]\Bigg\}\Bigg\}\cos(2n\theta)\Bigg\} \tag{23}$$

Similarly, the other two displacement components can also be obtained.

4. Solution Procedures

In order to match the external applied load with the internal stress field, the external applied load is expanded in Bessel-Fourier series. In particular, Eq. (4) can also be written as

$$\sigma_{rr} = -\frac{F}{\pi R} - \sum_{n=1}^{\infty}\frac{2F}{n\pi b}J_1(\frac{2nb}{R})\cos 2n\theta \tag{24}$$

In addition, we rewrite all expressions for stresses (except for $\sigma_{\theta\theta}$) in a unified Bessel-Fourier series, and then specialize them on the curved surface as well as on the two end surfaces. By comparing the expressions for stresses with those by boundary conditions, we can derive a system of equations for the unknown coefficients. Subsequently, all unknown coefficients can be solved from these equations.

In particular, rewriting Eq. (17) and comparing it with Eq. (24) lead to

$$(2\nu-1)C_0 + \nu A_0 = -\frac{F}{\pi R} \tag{25}$$

$$-2n(2n-1)E_{0n}R^{2n-2} + H_{0n}[\nu(8n+4) - (4n^2+6n+2)R^{2n}] + \sum_{s=1}^{\infty} J_{2n}(\gamma_s R) \times\Bigg\{C_{sn}[1-\frac{4n^2}{\gamma_s^2 R^2}]\Gamma_s^{(0)} + D_{sn}[2\nu + (1-\frac{4n^2}{\gamma_s^2 R^2})]\Lambda_s^{(0)} + \frac{2nF_{sn}\Gamma_s^{(0)}}{\gamma_s^2 R^2}\Bigg\} = \Re_n \tag{26}$$

$$A_{mn}[2\nu I_{2n}(\eta_m R)-\frac{2}{\eta_m^2}\frac{\partial^2 I_{2n}(\eta_m R)}{\partial r^2}-\frac{R}{\eta_m^2}\frac{\partial^3 I_{2n}(\eta_m R)}{\partial r^3}]-\frac{B_{mn}}{\eta_m^2}\frac{\partial^2 I_{2n}(\eta_m R)}{\partial r^2}$$
$$+\frac{2nE_{mn}}{\eta_m^2}[\frac{I_{2n}(\eta_m R)}{R^2}-\frac{1}{R}\frac{\partial I_{2n}(\eta_m R)}{\partial r}]+\sum_{s=1}^{\infty}J_{2n}(\gamma_s R)\Big\{C_{sn}[1-\frac{4n^2}{\gamma_s^2 R^2}]\Gamma_{sm}^{(1)}+D_{sn}[2\nu\Gamma_{sm}^{(1)} \quad (27)$$
$$+(1-\frac{4n^2}{\gamma_s^2 R^2})(\Gamma_{sm}^{(1)}+\Lambda_{sm}^{(1)})]+\frac{2nF_{sn}}{\gamma_s^2 R^2}\Gamma_{sm}^{(1)}\Big\}=0$$

where the expressions of $\Gamma_s^{(0)}$, $\Lambda_s^{(0)}$, $\Gamma_{sm}^{(1)}$ and $\Lambda_{sm}^{(1)}$ are given in Appendix A, and

$$\Re_n=-\frac{2F}{n\pi b}J_1(\frac{2nb}{R}) \quad (28)$$

By applying the shear traction free condition given in Eq. (3) to Eq. (20), we have

$$2n(8n+4)(1-\nu)H_{0n}R^{2n-1}\Gamma_m^{(3)}+\frac{A_{mn}}{\eta_m}[(3-2\nu)\frac{\partial I_{2n}(\eta_m R)}{\partial r}+R\frac{\partial^2 I_{2n}(\eta_m R)}{\partial r^2})]+\frac{B_{mn}}{\eta_m}\frac{\partial I_{2n}(\eta_m R)}{\partial r}$$
$$+\frac{nE_{mn}}{\eta_m R}I_{2n}(\eta_m R)-\sum_{s=1}^{\infty}\frac{nF_{sn}}{\gamma_s R}J_{2n}(\gamma_s R)\Gamma_{sm}^{(2)}=0 \quad (29)$$

where the expressions of $\Gamma_{sm}^{(2)}$ and $\Gamma_m^{(3)}$ are given in Appendix A.

Applying the boundary condition given in Eq. (2) to Eq. (22) (i. e. $\sigma_{r\theta}=0$ on $r = R$) leads to

$$2n(2n-1)E_{0n}R^{2n-2}+2n(2n+1)H_{0n}R^{2n}$$
$$+\sum_{s=1}^{\infty}J_{2n}(\gamma_s R)\Big\{(\frac{4n^2}{\gamma_s^2 R^2}-\frac{1}{2})F_{sn}\Gamma_s^{(0)}-C_{sn}\frac{2n\Gamma_s^{(0)}}{\gamma_s^2 R^2}-D_{sn}\frac{2n(\Gamma_s^{(0)}+\Lambda_s^{(0)})}{\gamma_s^2 R^2}\Big\}=0 \quad (30)$$

$$\frac{2nA_{mn}}{\eta_m^2}\frac{\partial^2 I_{2n}(\eta_m R)}{\partial r^2}+\frac{2nB_{mn}}{\eta_m^2}[\frac{1}{R}\frac{\partial I_{2n}(\eta_m R)}{\partial r}-\frac{1}{R^2}I_{2n}(\eta_m R)]+\frac{E_{mn}}{2\eta_m^2}[-\frac{1}{R}\frac{\partial I_{2n}(\eta_m R)}{\partial r}+\frac{4n^2}{R^2}I_{2n}(\eta_m R)$$
$$+\frac{\partial^2 I_{2n}(\eta_m R)}{\partial r^2}]+\sum_{s=1}^{\infty}J_{2n}(\gamma_s R)\Big\{-\frac{2n}{\gamma_s^2 R^2}[C_{sn}\Gamma_{sm}^{(1)}+D_{sn}(\Gamma_{sm}^{(1)}+\Lambda_{sm}^{(1)})]+\frac{4n^2F_{sn}\Gamma_{sm}^{(1)}}{\gamma_s^2 R^2}\Big\}=0 \quad (31)$$

where the expressions of $\Gamma_s^{(0)}$ and $\Lambda_s^{(0)}$ are given in Appendix A.

The boundary condition $\sigma_{zz}=0$ on the two end surfaces $z=\pm h$ (the first of Eq. (1)) leads to

$$2(2-\nu)C_0+(1-\nu)A_0=0 \quad (32)$$

$$H_{0n}(2-\nu)(8n+4)P_{sn}+\sum_{m=1}^{\infty}\{A_{mn}[(4-2\nu-2n)T_{sm}+U_{sm}]+B_{mn}T_{sm}\}(-1)^m$$
$$-C_{sn}\cosh(\gamma_s h)-D_{sn}[(2\nu-1)\cosh(\gamma_s h)+\gamma_s h\sinh(\gamma_s h)]=0 \tag{33}$$

where the expressions of P_{sn}, T_{sm} and U_{sm} are given in Appendix A.

The boundary condition $\sigma_{zr}=0$ on the two end surfaces $z=\pm h$ leads to

$$2n(8n+4)(1-\nu)H_{0n}P_{sn}\gamma_s h-nF_{sn}\sinh(\gamma_s h)$$
$$-\sum_{m=1}^{\infty}\frac{\gamma_s V_{sn}}{\gamma_m}\{C_{mn}\sinh(\gamma_m h)+D_{mn}[2\nu\sinh(\gamma_m h)+\gamma_m h\cosh(\gamma_m h)]\}=0 \tag{34}$$

where s is an integer greater than zero, and the expression of V_{sn} is given in Appendix A.

The boundary condition $\sigma_{z\theta}=0$ on the two end surfaces $z=\pm h$ leads to

$$-2n(8n+4)(1-\nu)H_{0n}P_{sn}\gamma_s h+2nC_{sn}\sinh(\gamma_s h)+2nD_{sn}[2\nu\sinh(\gamma_s h)+\gamma_s h\cosh(\gamma_s h)]$$
$$+\sum_{m=1}^{\infty}\frac{\gamma_s V_{sn}}{2\gamma_m}F_{mn}\sinh(\gamma_m h)=0 \tag{35}$$

By now, all boundary conditions have been considered, and all unknown coefficients can be uniquely determined. More specifically, the unknown constants A_0 and C_0 can be solved from Eqs. (25) and (32), whereas $E_{0n}, H_{0n}, A_{mn}, B_{mn}$, E_{mn}, C_{sn}, D_{sn} and F_{sn} can be solved from the coupled system of equations Eqs. (26-27), (29-31), and (33-35). For example, if the number of truncated terms selected for indices *m, n* and *s* equals a finite integer *q*, the number of unknowns for $E_{0n}, H_{0n}, A_{mn}, B_{mn}$, E_{mn}, C_{sn}, D_{sn} and F_{sn} becomes $2(q+1)+6q(q+1)$. It is clear from Eqs. (26-27), (29-31), and (33-35) that the number of equations is also exactly $2(q+1)+6q(q+1)$. Numerical results of the present analytical solutions are given and discussed in the next section.

5. Numerical Results and Discussions

The determination of the unknown coefficients by the boundary conditions in the last section involves the solution of a system of simultaneous equations in terms of infinite series.

In actual computation, the infinite series has to be truncated and only finite number of terms is retained. However, our numerical calculations show that the system of equations for solving $E_{0n}, H_{0n}, A_{mn}, B_{mn}, E_{mn}, C_{sn}, D_{sn}$ and F_{sn} becomes ill-conditioned for large *m* and *s*.

It is observed that coefficients of the system of equations including cosh, sinh, and I_{2n} (modified Bessel function) increase exponentially with argument (or indirectly increase with *m* and *s*), whereas coefficients for other terms involving only sine, cosine, and J_{2n} (Bessel function) are simply oscillating functions with finite value even for large *m* and *s*. This is the cause of ill-conditioning of this system of equations as we increase *m* and *s*.

We found that the ill-condition can be alleviated by a proper scaling of the coefficients. In particular, we divide all coefficients for A_{mn}, B_{mm} and E_{mn} with the modified Bessel function $I_{2n}(\eta_m R)$ because they cause ill-conditioning for large *m*. That is, automatically all constants A_{mn}, B_{mm} and E_{mn} have been scaled by multiplying $I_{2n}(\eta_m R)$. We divide all coefficients for C_{sn}, D_{sn} and F_{sn} with $\cosh(\gamma_s h)$ because they cause ill-conditioning for large *s*. That is, automatically all constants C_{sn}, D_{sn} and F_{sn} have been scaled by multiplying $\cosh(\gamma_s h)$. After solving $E_{0n}, H_{0n}, A_{mn}, B_{mn}, E_{mn}, C_{sn}$, D_{sn} and F_{sn}, the final solutions of A_{mn}, B_{mn} and E_{mn} can be obtained by dividing them with $I_{2n}(\eta_m R)$ while the solutions for C_{sn}, D_{sn} and F_{sn} can be obtained by dividing them with $\cosh(\gamma_s h)$.

Since the actual applied normal stress of the boundary condition (4) on the curved surface is a nonlinear function of the applied force and the modulus of the cylinder as shown in Eq. (5) (due to the inclusion of Hertz contact), the final stress distribution cannot be normalized linearly with respect to the applied load and modulus, like other linear elastic stress analyses. Therefore, in this paper typical values of rock tested complying with the ISRM (1978) standard and of bituminous material or asphalt tested complying with the ASTM (2004)

standard will be adopted in the following numerical calculations. Our choice of rock and asphalt should cover both strong and weak solids.

5.1. *The contact width and angle versus tested material and testing method*

Figures 2(a) and 2(b) plot the contact width b versus the applied line force F (MN/m) for various values of Poisson's ratio for a typical rock of Young's modulus of 50 GPa subjected to ISRM (1978) indirect tensile test and for a typical bituminous material of Young's modulus of 85 MPa subjected to ASTM (2004) indirect tensile test. These values are considered typical for rocks (Goodman, 1989) and for asphalts (Croney and Croney, 1998). The numerical results were obtained by using Eq. (5) with the special case of rigid platens (i.e. $\bar{E} \to \infty$), and the effect non-rigid loading platen will be considered later in Section 5.3. As suggested in ISRM (1978), the diameter of the rock cylinder is 54 mm, whereas the diameter of the bituminous material cylinder is 101.6 mm recommended in ASTM (2004). For typical rocks of moderate tensile strength, splitting failure occurs at around F = 0.5MN/m (roughly corresponding to a tensile strength of 6 MPa) whereas for typical asphalts of moderate tensile strength, splitting failure occurs at around F = 0.05MN/m (roughly corresponding to a tensile strength of 0.3 MPa), shown as vertical dotted lines in Fig. 2. These values of line forces will be used in later numerical calculations. At these force values, the contact widths are about 2 mm and 12 mm for the ISRM test on rock and ASTM test on asphalt. Figure 3 plots the contact angles versus the applied force F for various values of Poisson's ratio. These contact angles are needed for later stress comparisons with the 2-D solutions because the classical 2-D Hondros (1959) solution is expressed in terms of the contact angle (or $2\theta_0$), as shown in Appendix B. In general, contact angles at the chosen applied forces of 0.5 MN/m for rocks and 0.05 MN/m for asphalts are around 4° to 12°.

5.2. *The convergence of the present solution*

In order to check the convergence of the present 3-D analytical solution, Fig. 4 plots the hoop stresses at the center of the cylinder (i.e. $r/R = z/h = 0$) versus H/D for $\nu = 0.35$ and for various numbers of summation terms (n, s, and m) used in the series solutions of the displacement functions given in Eqs. (15-16). The height $H = 2h$ and diameter $D = 2R$ are defined in Fig. 1. The size of the cylinder and other mechanical properties for rocks (ISRM test) and asphalts (ASTM test) are the same as those used in Fig. 2. The hoop stress has been normalized with respect to Hertz 2-D solution, $\sigma_0 = 2F/(\pi D)$. Note that the contact widths b for ISRM results and ASTM results are not the same because of different shape of the loading platens being used. The average value of Poisson's ratio of rocks and asphalts is about 0.35 (e.g. Goodman, 1989; Table 3 of Chau and Wong, 1996; Croney and Croney, 1998; Low et al., 1993), and thus this value was used in the plots. As discussed earlier, the coefficients of the system of equations for unknowns $E_{0n}, H_{0n}, A_{mn}, B_{mn}$, E_{mn}, C_{sn}, D_{sn} and F_{sn} become very large for large m and s. Therefore, we should not be too greedy in calculating the number of terms. Nevertheless, Fig. 4 shows that the hoop stresses converge very quickly to a steady value when more than 20 terms are used for each of n, s, and m. The solutions for 20 terms for n, s, and m or more are virtually indistinguishable for the hoop stress at $H/D = 0.5$, which is the value suggested by both ISRM and ASTM standards. Figure 5 plots the hoop stresses versus r/R for $\nu = 0.35$, $\theta = 0$, $z/h = 0$, and $H/D = 0.5$ and for various numbers of summation terms (n, s, and m) used in the series solutions given in Eqs. (15-16) for the displacement functions. It is clear that the solutions for 20 terms or more for n, s, and m are virtually the same, independent of the value of r/R. Therefore, in all of the following calculations, numerical results are obtained by using 50 terms of n, s and m.

5.3. *The effect of loading platen stiffness on stress concentration*

So far, we have assumed that the loading platen is rigid comparing to the tested materials. To illustrate the effect of non-rigid loading platen, Fig. 6 plots the normalized hoop stress along the normalized radial distance (r/R) for various values of Poisson's ratio and for both rigid and elastic loading contacts. All parameters are the same as those used in Figs. 2-4. The results are obtained for the ISRM test. Young's modulus $\bar{E}$ of the loading steel platen given in Eq. (5) is assumed as 210 GPa whilst the Poisson's ratios being the same as those of the tested cylindrical material. The solutions for rigid contact are plotted as solid lines whereas the elastic solutions are shown as circles. These solutions are essentially indistinguishable in Fig. 6, and thus it appears that the loading platen can be assumed as rigid. However, it should be cautious that this observation is only true for the present case of frictionless contact (or smooth contact). Recently, Kourkoulis et al. (2013) showed that frictional stress at contact in Brazilian test may strongly influence the length of contact for the case of stick contact (no slip contact or stick condition). For such cases, the magnitude of contact stress can be highly sensitive to the relative stiffness of the loading lateens and the specimens (see Figure 7 of Kourkoulis et al., 2013). The validity of the predictions of displacements and strains by Kourkoulis et al. (2013) were also verified experimentally by "digital image correlation" (DIC) method (Kourkoulis et al., 2012). Although Kourkoulis et al. (2013) did not demonstrate how the loading platen stiffness influences the maximum tensile stress within the cylinder, apparently it is not negligible as in the present case of frictionless contact. Further studies are clearly needed on frictional contact.

5.4. *Comparison with two dimensional solutions by Hertz in 1883 and Hondros (1959)*

The 2-D analytical solutions obtained by Hertz in 1883 for the case of line loads (see Timoshenko and Goodier, 1982) and by Hondros (1959) for the case of radial strip loads have been extensively used in estimating the tensile strength of brittle materials. Figure 7 shows

the comparisons of the present 3-D solution with the 2-D classical solution by Hondros (1959) for the normalized hoop stress $\sigma_{\theta\theta}/\sigma_0$ [where $\sigma_0 = 2F/(\pi D)$ is the Hertz 2-D solution for the hoop stress] and for the normalized radial stress σ_{rr}/σ_0 at the center of the cylinder against *r/R* for various values of Poisson's ratio ν. The plot is calculated for *H/D* = 0.5. Note that the 2-D solution is independent of ν. Both the normalized hoop stress $\sigma_{\theta\theta}/\sigma_0$ and the normalized radial stress σ_{rr}/σ_0 at the center of the cylinder obtained by the present 3-D solution approach the classical 2-D solutions for $\nu \to 0$, and thus Fig. 7 demonstrates the validity of the present solution. Similar to Hondros (1959) solution, the present 3-D hoop stress is tensile only in the middle portion of the circular section and becomes highly compressive when the contact platens are approached. Such edge stress singularity in circular cylinders was considered by Roberts and Keer (1978) but is out of the scope of the present study. This compressive zone under the contact is absent in the classical Hertz's line load solution, which predicts a uniform tensile hoop across the diametral line between the loading platens (Timoshenko and Goodier, 1982).

5.5. *Three dimensional nature of the hoop stress*

To illustrate the 3-D nature of the present solution, Fig. 8 plots the normalized hoop stress $\sigma_{\theta\theta}/\sigma_0$ versus the normalized distance *r/R* for ν = 0.35, θ = 0 and for various values of *z/h*. The tensile hoop stress in the middle portion of the diameter joining the two contact platens increases with *z/h* from 0 to 0.7. Comparison of Figs. 7 and 8 reveals that the 3-D hoop stress is actually larger than the 2-D solution away from the center of the cylinder for the case of ν = 0.35 (i.e. $z/h \neq 0$). It is also clear from Fig. 8 that the concave contact platen of ISRM standard produces a larger tensile zone in the middle part of the cylinder than that induced by the flat platen of ASTM standard. Figure 8 shows that the maximum tensile stress mainly appears at

the center of the cylinder (i.e. $r/R = 0$) for z/h smaller than 0.7 for both ISRM and ASTM indirect tensile tests. Even for the case of ISRM test at $z/h = 0.7$, the tensile stress at the center is only slightly smaller than the maximum value at about $r/R = 0.6$. Therefore, in the subsequent calculations we will focus on the stress concentration along the axis (i.e. $r/D = 0$) of the cylinder.

Figure 9 plots the 3-D normalized hoop stress $\sigma_{\theta\theta} / \sigma_0$ along the axis of the cylinder z/h for various value of ν (i.e. $r/R = 0$). The hoop stress for $z/h < (z/h)_{cr}$ (≈ 0.56) decreases with ν whereas it increases with ν for $z/h > (z/h)_{cr}$. Note that the critical $(z/h)_{cr}$ is roughly the same for both ISRM and ASTM standards. At this critical section along the axis, the hoop stress is independent of Poisson's ratio and equals the 2-D Hertz solution or the 2-D Hondros (1959) solution. Note that the 2-D Hondros (1959) solutions shown in Figs. 9 and 10 for ISRM and ASTM cases are not the same. It is because the contact angle θ_0 depends on the contact width b determined from Eq. (5), and consequently the contact width is not the same for ISRM and ASTM tests for cylinders of different diameters. This difference in θ_0, in turn, affects the hoop stress evaluated from Eqs. (B1) and (B2) given in Appendix B for the 2-D Hondros (1959) solution. Consequently, the 2-D solutions are not the same in Figs. 9 and 10.

More importantly, the 2-D solution fails to capture the peaks of the hoop stress at around $z/h = 0.8$ as shown in Fig. 9. The plots in Fig. 8 also suggest that splitting of the cylinder is likely to initiate from the ends of the cylinder, instead of from the center of the cylinder. This result agrees qualitatively with the FEM results of Yu et al. (2006). Figure 10 plots the normalized compressive radial stress σ_{rr} / σ_0 along the axis of the cylinder z/h for various value of ν (i.e. $r/R = 0$). As expected, the 2-D Hondros (1959) solution is independent of the value of z/h. For z/h smaller than the critical value of $(z/h)_{cr}$ (≈ 0.56), the radial compressive stress in general decreases with ν, but increases with ν for z/h larger than the critical value. Similar to Fig. 9, at the critical value of z/h the radial stress equals the 2-D Hondros (1959)

solution. Again, the 2-D solution fails to capture the maximum radial stress near the end surfaces of the cylinder. Therefore, it is important to investigate the maximum stress concentration within the cylinder under indirect tensile test using 3-D solution.

5.6. The maximum tensile hoop stress within the cylinder

Figure 9 demonstrates that the maximum hoop stress roughly appears in the range: $0.7 < z/h < 0.8$ along the axis of the cylinder. However, the plots of hoop stress given in Figs. 8 and 9 are only for the geometric ratio $H/D = 0.5$ recommended by the ISRM and ASTM standards. Therefore, Fig. 11 plots the maximum tensile stress (solid lines with data point) within the cylinder together with the tensile stress at the center ($r/R = 0$) (solid lines) versus H/D for various values of ν. Note that the incompressible limit of $\nu = 0.5$ will lead to mathematical singularity in the stress analysis; thus, a value of $\nu = 0.4995$ has been used to approximate the incompressible limit. The dotted line is the 2-D Hondros (1959) solution whereas the left diagram is for ISRM setup on rocks and the right diagram is for ASTM setup on asphalts. Similar to the conclusion for Fig. 9, the maximum tensile stress near the end surface increases with ν while the tensile stress at center decreases with ν. The hoop stress at the center approaches the 2-D solution for both $H/D \to 0$ and $H/D \to \infty$ whereas the maximum hoop stress increases monotonically with H/D and ν. It is clear from Fig. 11 that the 3-D effect is of utmost importance in identifying the maximum value of tensile hoop in the cylinder under indirect tensile test. For long cylinders (say $H/D = 2.3$), the error of the maximum tensile stress may be as large as 20% to 60%, depending on the value of Poisson's ratio. For the case of $\nu = 0.4995$, the errors of the hoop stress at the center of the cylinder reach 27% and 15% at $H/D = 1.0$ and $H/D = 0.5$, respectively. The errors are relatively insensitive to whether the ISRM or ASTM method is used. Figure 12 plots that the location of the maximum tensile stress versus H/D for various values of Poisson's ratio. When $\nu = 0.1$ and $H/D = 0.3$, the

maximum tensile stress appears at the center of the cylinder (z/h = 0). More generally, the maximum tensile hoop stress appears near the end surfaces (z/h = 1.0) rather than at the center of the axis for Poisson's ratio larger than 0.1 and when H/D > 0.3. For H/D = 0.5 recommended by the ISRM and ASTM standards, the maximum tensile stress typically appears at $z/h \approx 0.7$~0.9. Therefore, the 2-D solution fails to capture maximum hoop stress off the center of the cylinder, especially for long cylinders.

6. Conclusion

A 3-D analytical solution for solid finite elastic cylinders subjected to the indirect tensile test is obtained. The present solution can be considered as the 3-D counterpart of the classical 2-D solution obtained by Hertz in 1883 (see Timoshenko and Goodier, 1982) and by Hondros (1959). The applied loads induced by interaction between the cylinder and the loading platens are modeled by using Hertz contact, for both concave platens of ISRM (1978) and flat platens of ASTM (2004) standard. As expected, Hertz contact theory leads to a contact width being a nonlinear function of the applied load, the size and shape of the specimen, and the elastic properties of the specimen. The equilibrium equations are solved by using two displacement functions. The general solution forms of these displacement functions are expressed in series of Bessel functions, hyperbolic functions and trigonometric functions. By applying Fourier-Bessel series expansion technique, all the boundary conditions are satisfied exactly.

One strong material (a typical rock with Young's modulus of 50 GPa) under ISRM (1978) standard and one weak material (typical asphalts with Young's modulus of 85 MPa) were considered. For typical rock cylinders under ISRM indirect tensile tests, the contact width ranges from 1.2 mm to 2.6 mm (or corresponding to a contact angle ranges from 2.4° to 6°), depending on the actual value of Poisson's ratio and the applied force. For typical asphalt cylinders under ASTM indirect tensile tests, the contact width ranges from 8mm to 16mm (or

corresponding to a contact angle ranges from 8° to 20°), depending on the actual value of Poisson's ratio and applied force. The convergence of the series solution is checked and 50 terms in both Fourier and Fourier-Bessel series expansions are found sufficient to give converged solutions. The difference in the hoop stress and radial stress between the 2-D Hertz solution or the 2-D Hondros (1959) solution and the present 3-D solution increases with *H/D* ratio as well as Poisson's ratio (ν). For the case of frictionless contact, the effect of loading platen stiffness on tensile stress in cylinders appears to be negligible (i.e. loading platens can be viewed as rigid). For the recommended *H/D* = 0.5, the error in tensile strength may be up to 15% for both rocks and asphalts, whereas for larger *H/D* up to 2.0 the error ranges from 15% (highly compressible solid with ν = 0.1) to 60% (nearly incompressible solid with ν = 0.4995) for both materials. In general, the error of the 2-D solutions in the normalized stress is roughly independent of the experimental setup (whether ISRM or ASTM standard) and independent of the strength of the material (whether rocks or asphalts). In short, the 2-D solution in general underestimates the tensile stress and cannot predict the location of the maximum hoop stress which typically locates close to the end surface of the cylinder.

The current practice of using specimens of shape of *H/D* = 0.5, as suggested by ASTM (2004) and ISRM (1978), does not warrant the use of 2-D solution either the Hertz solution in 1883 (Timoshenko and Goodier, 1982) or Hondros (1959) solutions. It seems that major revision is needed in the current code of practice to reflect the inaccurate prediction of indirect tensile strength using the 2-D solution. One simple way to remedy the problem is to introduce a correction factor (based on the present 3-D solution) to the classical 2-D solution as a function of shape of the cylinder and Poisson's ratio of the material.

In summary, the present study should provide a useful solution and theoretical basis in allowing us to better interpret the tensile strength of solids under indirect tensile test. Although the present analysis is valid only for elastic materials, for most brittle materials (like

brittle rocks) there is not much nonlinear response before the splitting fracture of the specimen. Therefore, the present analysis is useful in strength interpretation.

Acknowledgments

This work was supported by the National Natural Science Foundation of China (Grant No. 11272049 and 11032003) and by a grant from The Hong Kong Polytechnic University (Project No. 1-BBZF). The works by Kourkoulis and coauthors on the effect of frictional contact were brought to our attention by Professor D.A. Hills.

Appendix A: Expressions for $\Gamma_s^{(0)}$, $\Lambda_s^{(0)}$, $\Gamma_{sm}^{(1)}$, $\Lambda_{sm}^{(1)}$, $\Gamma_{sm}^{(2)}$, $\Gamma_m^{(3)}$ P_{sn}, T_{sm}, U_{sm}, and V_{sn}

$$\Gamma_s^{(0)} = \frac{\sinh(\gamma_s h)}{\gamma_s h} \tag{A1}$$

$$\Lambda_s^{(0)} = \frac{\sinh(\gamma_s h)}{\gamma_s h}[\gamma_s h\cosh(\gamma_s h) - \sinh(\gamma_s h)] \tag{A2}$$

$$\Gamma_{sm}^{(1)} = \frac{2\gamma_s(-1)^m \sinh(\gamma_s h)}{h(\gamma_s^2 + \eta_m^2)} \tag{A3}$$

$$\Lambda_{sm}^{(1)} = \frac{2\gamma_s(-1)^m \sinh(\gamma_s h)}{h(\gamma_s^2 + \eta_m^2)}[\gamma_s h\cosh(\gamma_s h) + \frac{\eta_m^2 - \gamma_s^2}{\gamma_s^2 + \eta_m^2}\sinh(\gamma_s h)] \tag{A4}$$

$$\Gamma_{sm}^{(2)} = \frac{2\eta_m(-1)^{m+1} \sinh(\gamma_s h)}{h(\gamma_s^2 + \eta_m^2)} \tag{A5}$$

$$\Gamma_m^{(3)} = \frac{2(-1)^{m+1}}{\eta_m} \tag{A6}$$

$$P_{sn} = \frac{2\lambda_s R^{2n} J_{2n+1}(\lambda_s)}{(\lambda_s^2 - 4n^2)J_{2n}^2(\lambda_s)} \tag{A7}$$

$$T_{sm} = \frac{2\lambda_s^2}{(\lambda_s^2 - 4n^2)[(\eta_m R)^2 + \lambda_s^2]J_{2n}^2(\lambda_s)}[\eta_m R I_{2n+1}(\eta_m R)J_{2n}(\lambda_s) + \lambda_s I_{2n}(\eta_m R)J_{2n+1}(\lambda_s)] \tag{A8}$$

$$U_{sm}=\frac{2\lambda_s^2\eta_m R}{(\lambda_s^2-4n^2)[(\eta_m R)^2+\lambda_s^2]J_{2n}^2(\lambda_s)}\left\{\frac{2(2n-1)\eta_m R}{(\eta_m R)^2+\lambda_s^2}[\eta_m R I_{2n+1}(\eta_m R)J_{2n}(\lambda_s)\right.$$
$$+\lambda_s I_{2n}(\eta_m R)J_{2n+1}(\lambda_s)]+\frac{4n\lambda_s}{(\eta_m R)^2+\lambda_s^2}[\eta_m R I_{2n}(\eta_m R)J_{2n-1}(\lambda_s)+\lambda_s I_{2n-1}(\eta_m R)J_{2n}(\lambda_s)] \quad \text{(A9)}$$
$$\left.+\eta_m R I_{2n}(\eta_m R)J_{2n}(\lambda_s)-\lambda_s I_{2n-1}(\eta_m R)J_{2n-1}(\lambda_s)\right\}$$

If $\lambda_p \neq \lambda_s$, then

$$V_{sn}=\frac{2\lambda_s^2}{(\lambda_s^2-4n^2)(\lambda_p^2-\lambda_s^2)J_{2n}^2(\lambda_s)}\left\{\lambda_p^2 J_{2n}(\lambda_p)J_{2n}(\lambda_s)+\lambda_s\lambda_p J_{2n-1}(\lambda_p)J_{2n-1}(\lambda_s)\right.$$
$$-\frac{4n\lambda_p\lambda_s}{\lambda_p^2-\lambda_s^2}[\lambda_p J_{2n}(\lambda_p)J_{2n-1}(\lambda_s)-\lambda_s J_{2n-1}(\lambda_p)J_{2n}(\lambda_s)] \quad \text{(A10)}$$
$$\left.+\frac{2n(\lambda_p^2+\lambda_s^2)-2\lambda_p^2}{\lambda_p^2-\lambda_s^2}[\lambda_p J_{2n+1}(\lambda_p)J_{2n}(\lambda_s)-\lambda_s J_{2n}(\lambda_p)J_{2n+1}(\lambda_s)]\right\}$$

If $\lambda_p = \lambda_s$, then

$$V_{sn}=\frac{\lambda_s^2 J_{2n-1}(\lambda_s)J_{2n+1}(\lambda_s)}{(\lambda_s^2-4n^2)J_{2n}^2(\lambda_s)} \quad \text{(A11)}$$

Appendix B: 2-D solution by Hondros (1959)

The following stress components in polar coordinates were derived by Hondros (1959) for the diametral compression of a circular cylinder over a contact angle of $2\theta_0$:

$$\sigma_{rr}=\frac{2\theta_0 p}{\pi}+\frac{2p}{\pi}\sum_{m=1}^{\infty}\left(\frac{r}{R}\right)^{2m-2}\left\{1-\left(1-\frac{1}{m}\right)\left(\frac{r}{R}\right)^2\right\}\sin 2m\theta_0\cos 2m\theta \quad \text{(B1)}$$

$$\sigma_{\theta\theta}=\frac{2\theta_0 p}{\pi}-\frac{2p}{\pi}\sum_{m=1}^{\infty}\left(\frac{r}{R}\right)^{2m-2}\left\{1-\left(1+\frac{1}{m}\right)\left(\frac{r}{R}\right)^2\right\}\sin 2m\theta_0\cos 2m\theta \quad \text{(B2)}$$

$$\sigma_{r\theta}=\frac{2p}{\pi}\sum_{m=1}^{\infty}\left\{\left(\frac{r}{R}\right)^{2m}-\left(\frac{r}{R}\right)^{2m-2}\right\}\sin 2m\theta_0\sin 2m\theta \quad \text{(B3)}$$

where p is the uniform radial pressure applied over the arcs $-\theta_0 < \theta < \theta_0$ and $\pi - \theta_0 < \theta < \pi + \theta_0$ of the curved surface of the cylinder. This solution is used for comparison with our 3-D solution.

References

Abramowitz, M., Stegun, I. A., 1965. Handbook of Mathematical Functions, Dover, New York.

Akazawa, T., 1953. Tension test method for concrete. Bulletin No. 16, November 1953, The International Union of Testing and Research Laboratory for Material and Construction (RILEM Bulletin), Paris, France, pp. 13-23.

ASTM, 1995. Standard Test Method for Indirect Tension Test for Resilient Modulus of Bituminous Mixtures. D4123-82 (re-approved 1995 but withdrawn in 2003), pp. 423-425.

ASTM, 2004. Standard Test Method for Splitting Tensile Strength of Cylindrical Concrete Specimens. Designation: C 496/C 496M – 04, 1-5.

Bieniawski, Z.T., Hawkes, I., 1978. Suggested method for determining tensile strength of rock materials. Int. J. Rock Mech. Min. Sci. & Geomech. Abstr. 15(3), 99-103.

Carneiro, F.L.L.B., 1943. A new method to determine the tensile strength of concrete, in: Proceedings of the Fifth Meeting of the Brazilian Association for Technical Rules, pp. 126-129.

Carneiro, F.L.L.B., Barcellos, A., 1953. Tensile strength of concrete. RILEM Bulletin 13, 97-123.

Chau, K.T., 2013. Analytic Methods in Geomechanics, CRC Press, Roca Baton.

Chau, K.T., Wei, X.X., 2000. Finite solid circular cylinders subjected to arbitrary surface load: part I. Analytic solution. Int. J. Solids & Struct. 37(47), 5707-5732.

Chau, K.T., Wei, X.X., 2001. A new analytic solution for the diametral point load strength test on finite solid circular cylinders. Int. J. Solids & Struct. 38(9), 1459-1481.

Chau, K.T., Wong, R.H.C., 1996. Uniaxial compressive strength and point load strength of rocks. Int. J. Rock Mech. Min. Sci. & Geomech. Abstr. 33(2), 183-188.

Chen, A.C.T., Chen, W.F., 1976. Nonlinear analysis of concrete splitting tests. Comput. Struct. 6(6), 451-457.

Croney, D., Croney, P., 1998. Design and Performance of Road Pavements, third ed. McGraw Hill, New York.

Fairbairn, E.M.R., Ulm, F.-J., 2002. A tribute to Fernado L.L.B. Carneiro (1913-2001) engineer and scientist who invented the Brazilian Test. Material and Structures 35(April), 195-196.

Goodman, R.E., 1989. Introduction of Rock Mechanics, second ed. Wiley, New York.

Hobbs, D.B., 1965. An assessment of a technique for determining the tensile strength of rock. Brit. J. Appl. Phys. 16, 259-269.

Hondros, G., 1959. The evaluation of Poisson's ratio and the modulus of materials of a low tensile resistance by the Brazilian (indirect tensile) test with particular reference to concrete. Aust. J. Appl. Sci. 10, 243-268.

ISRM, 1978. Suggested methods for determining tensile strength of rock materials. Int. J. Rock Mech. Min. Sci. 15, 99-103.

Jaeger, J.C., Cook, N.G.W., 1976. Fundamentals of Rock Mechanics, second ed. Chapman and Hall, London.

Kourkoulis, S.K., Markides, Ch.F., Chatzistergos, P.E. 2012. The Brazilian disc under parabolically varying load: theoretical and experimental study of the displacement field. Int. J. Soilds & Struct. 49, 959-972.

Kourkoulis, S.K., Markides, Ch.F., Hemsley, J.A. 2013. Frictional stresses at the disc-jaw interface during the standardized execution of the Brazilian disc test. Acta Mech. 224, 255-268.

Little, R.W., 1973. Elasticity, Prentice Hall, Englewood Cliffs.

Low, B.H., Tan, S.A., Fwa, T.F., 1993. Analysis of Marshall test behavior with triaxial test determined material properties. J. Test. Eval. 21 (3), 192-198.

Machida, A., 1975. Studies on tests for splitting tensile strength of concrete. Proc. of JSCE, No. 242, October, 1975, 115-124.

Mamlouk, M.S., Yuan, Y.M., Tseng, N.T., Lee, G.C., 1983. Analysis of non-linear behavior of asphalt concrete during Marshall test. J. Test. Eval. 11(5), 327-332.

Muki, R., 1960. Asymmetric problems of the theory for a semi-infinite solid and a thick plate. In Progress in Solid Mechanics, ed. by I.N. Sneddon and R. Hill (North Holland, Amsterdam), Vol. 1, pp. 399–439.

Robert, M., Keer, L.M., 1987. An elastic circular-cylinder with displacement prescribed at the ends - axially-symmetrical case. Quart. J. of Mech. and Appl. Math. 40, 339-363.

Rocco, C, Guinea, G.V., Planas, J., Elices, M., 1999. Mechanisms of rupture in splitting tests. ACI Mater. J. 96(1), 52-60.

Rocco, C., Guinea, G.V., Planas, J., Elices, M., 2001. Review of the splitting-test standards from a fracture mechanics point of view. Cem. & Concrete Res. 31(2), 73-82.

Roque, R., Buttlar, W.G., 1992. The development of a measurement and analysis method to accurately determine asphalt concrete properties using the indirect tensile mode. Proc. Assoc. Asphalt Paving Technologists, Vol. 61, pp. 304-332.

Timoshenko, S.P., Goodier, J.N., 1982. Theory of Elasticity, third ed. McGraw-Hill, New York.

Webb, R.F., Burati, J.L.J., Hill, H.S.J., 1985. Effect of specimen thickness on Marshall test results. Transport. Res. Rec., 132-140.

Wei, X.X., Chau, K.T., 2000. Finite solid circular cylinders subjected to arbitrary surface load. Part II - Application to double-punch test. Int. J. Solids & Struct. 37(40), 5733-5744.

Wei, X.X., Chau, K.T., 2002. Analytic solution for finite transversely isotropic circular cylinders under the axial point load test. J. Engng. Mech. ASCE 128(2), 209-219.

Wei, X.X., Chau, K.T., Wong, R.H.C., 1999. Analytic solution for axial point load strength test on solid circular cylinders. J. Engng. Mech. ASCE 125(12), 1349-1357.

Yu, Y., Yin, J., Zhong, Z., 2006. Shape effect in the Brazilian tensile strength test and a 3D FEM correction. Int. J. Rock Mech. Min. Sci. 43, 623-627.

Figure captions:

Fig. 1. A finite solid circular cylinder subjected to the indirect tensile test: (a) ISRM Brazilian test; (b) Mathematical model; and (c) ASTM test.

Fig. 2. The half width *b* of the contact area versus the applied force *F* (MN/m) for various Poisson's ratio ν for both ISRM and ASTM testing procedures. The parameters used for ISRM Brazilian test are: $E = 50GPa$, $D = 2R = 54$ mm, $H = 0.5$D, $R_2 = -1.5$R. The parameters used for ASTM indirect tensile test are: $E = 85MPa$, $D = 2R = 101.6$ mm, $H = 0.5D$, and $R_2 \to \infty$. Rigid platen is assumed (i.e. $\bar{E} \to \infty$).

Fig. 3. The half contact angle θ_0 of the contact area versus the applied force *F* (MN/m) for various Poisson's ratio ν for both ISRM and ASTM testing procedures. The parameters used for ISRM and ASTM tests are the same as those used in Fig. 2.

Fig. 4. The normalized hoop tensile stresses $\sigma_{\theta\theta}/\sigma_0$ at the center of the cylinder subjected to both ISRM and ASTM tests for various values of *n*, *s*, *m* and $\nu = 0.35$, where $\sigma_0 = 2F/(\pi D)$ is the 2-D Hertz solution. The line forces used in ISRM and ASTM tests are $F = 0.5MN/m$ and $F = 0.05MN/m$, respectively.

Fig. 5. The normalized hoop stresses $\sigma_{\theta\theta}/\sigma_0$ versus *r/R* for various values of *n*, *s*, *m* for *z/h* = 0, $\theta = 0$ and $\nu = 0.35$ for both ISRM and ASTM testing procedures. Other parameters used are the same as Fig. 4.

Fig. 6. The normalized stresses $\sigma_{\theta\theta}/\sigma_0$ and σ_{rr}/σ_0 versus the normalized distance *r/R* for *z/h* = 0, $\theta = 0$, and for various Poisson's ratio ν subjected to both rigid platen condition and elastic platen condition. The plots are for ISRM contacts and parameters used are: $E = 50GPa$, $D = 2R = 54$mm, $H = 0.5D$, $R_2 = -1.5$R. The Young's modulus $\bar{E}$ of the loading platen is assumed as 210 GPa whilst the Poisson's ratio being the same as those of the tested cylindrical material.

Fig. 7. The normalized radial and hoop stresses σ_{rr}/σ_0 and $\sigma_{\theta\theta}/\sigma_0$ versus the normalized distance *r/R* for *z/h* = 0, $\theta = 0$ and changing values of Poisson's ratio ν. The present 3-D solution and 2-D classical solution by Hondros (1959) are plotted as solid lines and center lines, respectively. Other parameters used are the same as Fig. 4.

Fig. 8. The normalized hoop stress $\sigma_{\theta\theta}/\sigma_0$ versus *r/R* for various values of *z/h* for $\theta = 0$ and $\nu = 0.35$ for both ISRM and ASTM indirect tensile tests. Other parameters used are the same as Fig. 4.

Fig. 9. The normalized hoop stress $\sigma_{\theta\theta}/\sigma_0$ versus the normalized distance *z/h* for *r/R* = 0, $\theta = 0$, and various Poisson's ratio ν. The 2-D Hondros (1959) solutions are also included as center lines.

Fig. 10. The normalized radial stress σ_{rr}/σ_0 versus the normalized distance *z/h* for *r/R* = 0, $\theta = 0$, and various Poisson's ratio ν. The 2-D Hondros (1959) solutions are also included as center lines.

Fig. 11. The maximum normalized hoop stress $\sigma_{\theta\theta}/\sigma_0$ (solid lines with data points) and hoop stress at the center (solid lines) versus the height-to-diameter ratio *H/D* for various Poisson's ratio ν. The 2-D classical solution by Hondros (1959) are plotted as dotted lines.

Fig. 12. The location *z/h* where the maximum tensile hoop stress is induced versus the height-to-diameter ratio *H/D* for various Poisson's ratio ν.

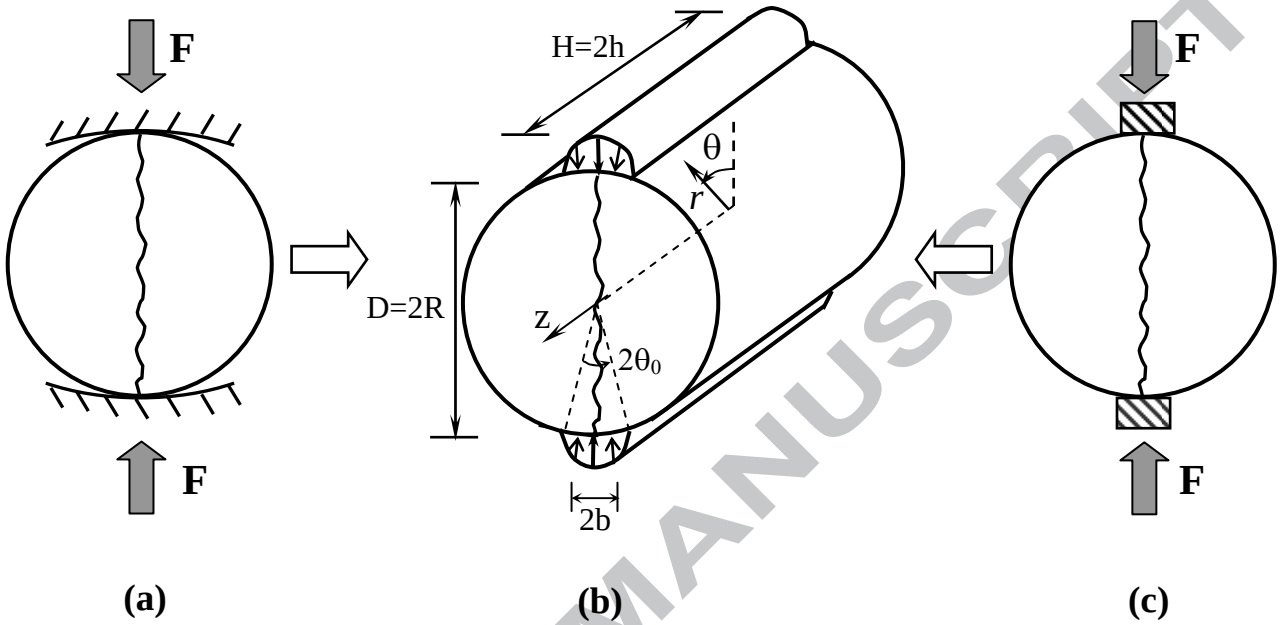

Fig. 1. A finite solid circular cylinder subjected to the indirect tensile test: (a) ISRM Brazilian test; (b) Mathematical model; and (c) ASTM test.

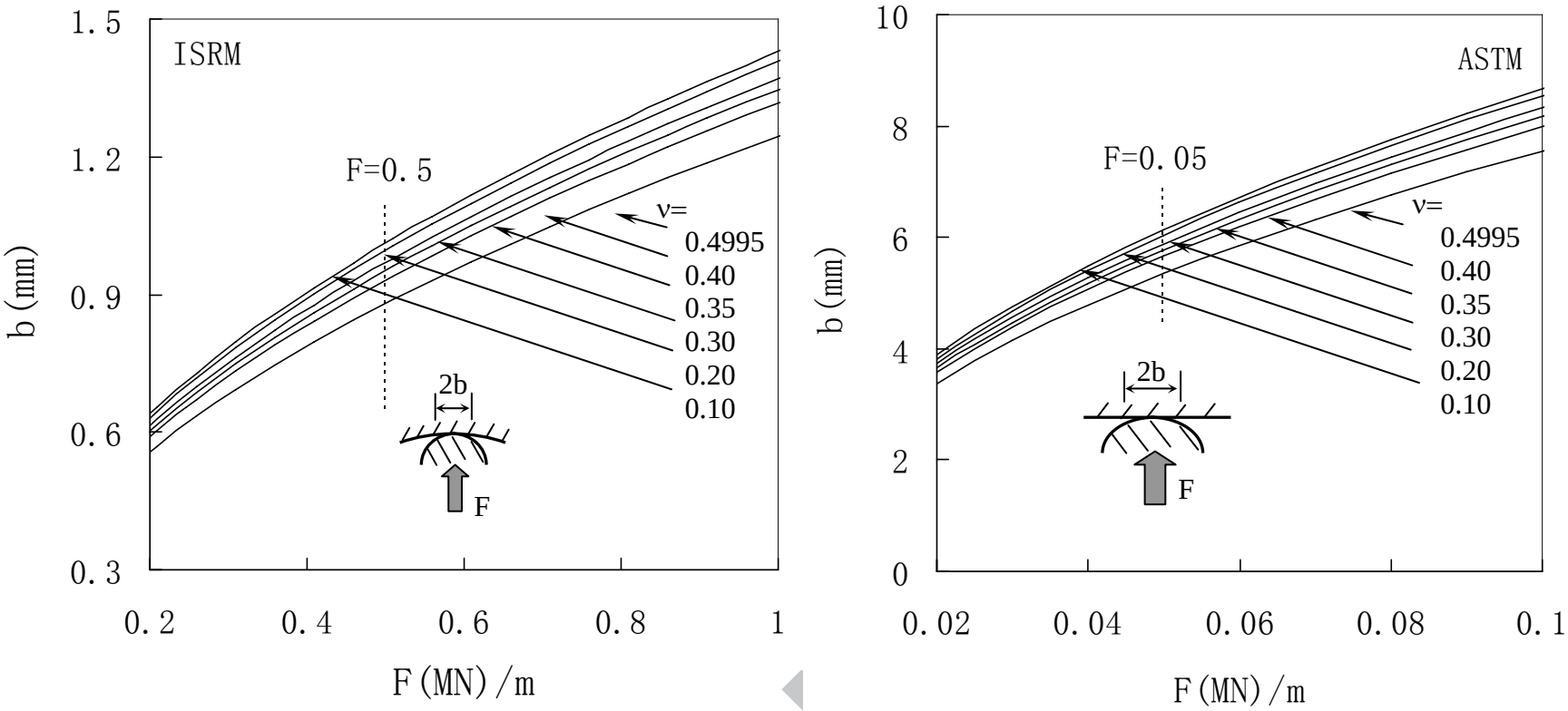

Fig. 2. The half width b of the contact area versus the applied force F (MN/m) for various Poisson's ratio ν for both ISRM and ASTM testing procedures. The parameters used for ISRM Brazilian test are: $E = 50GPa$, $D = 2R = 54$ mm, $H = 0.5$D, $R_2 = -1.5$R. The parameters used for ASTM indirect tensile test are: $E = 85MPa$, $D = 2R = 101.6$ mm, $H = 0.5D$, and $R_2 \to \infty$. Rigid platen is assumed (i.e. $\bar{E} \to \infty$).

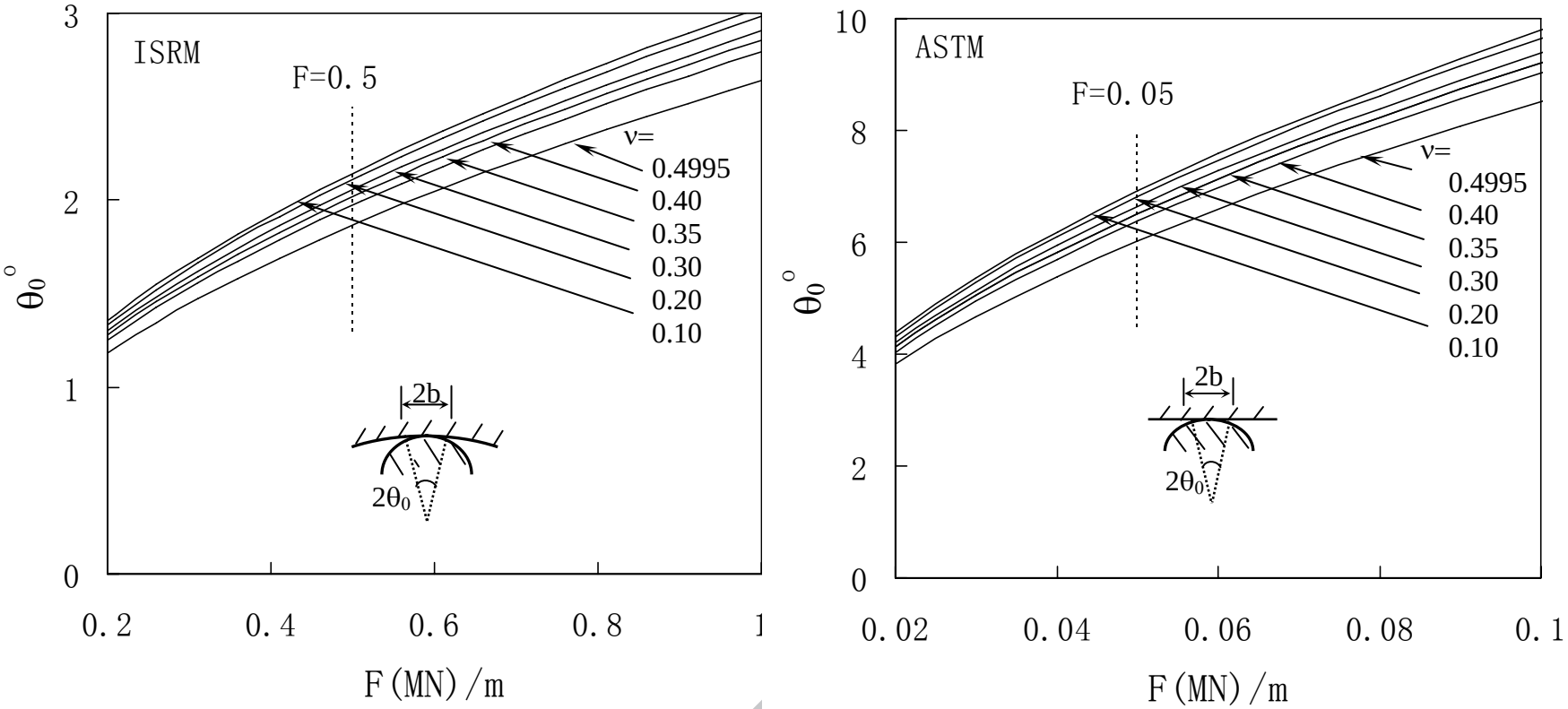

Fig. 3. The half contact angle θ_0 of the contact area versus the applied force F (MN/m) for various Poisson's ratio ν for both ISRM and ASTM testing procedures. The parameters used for ISRM and ASTM tests are the same as those used in Fig. 2.

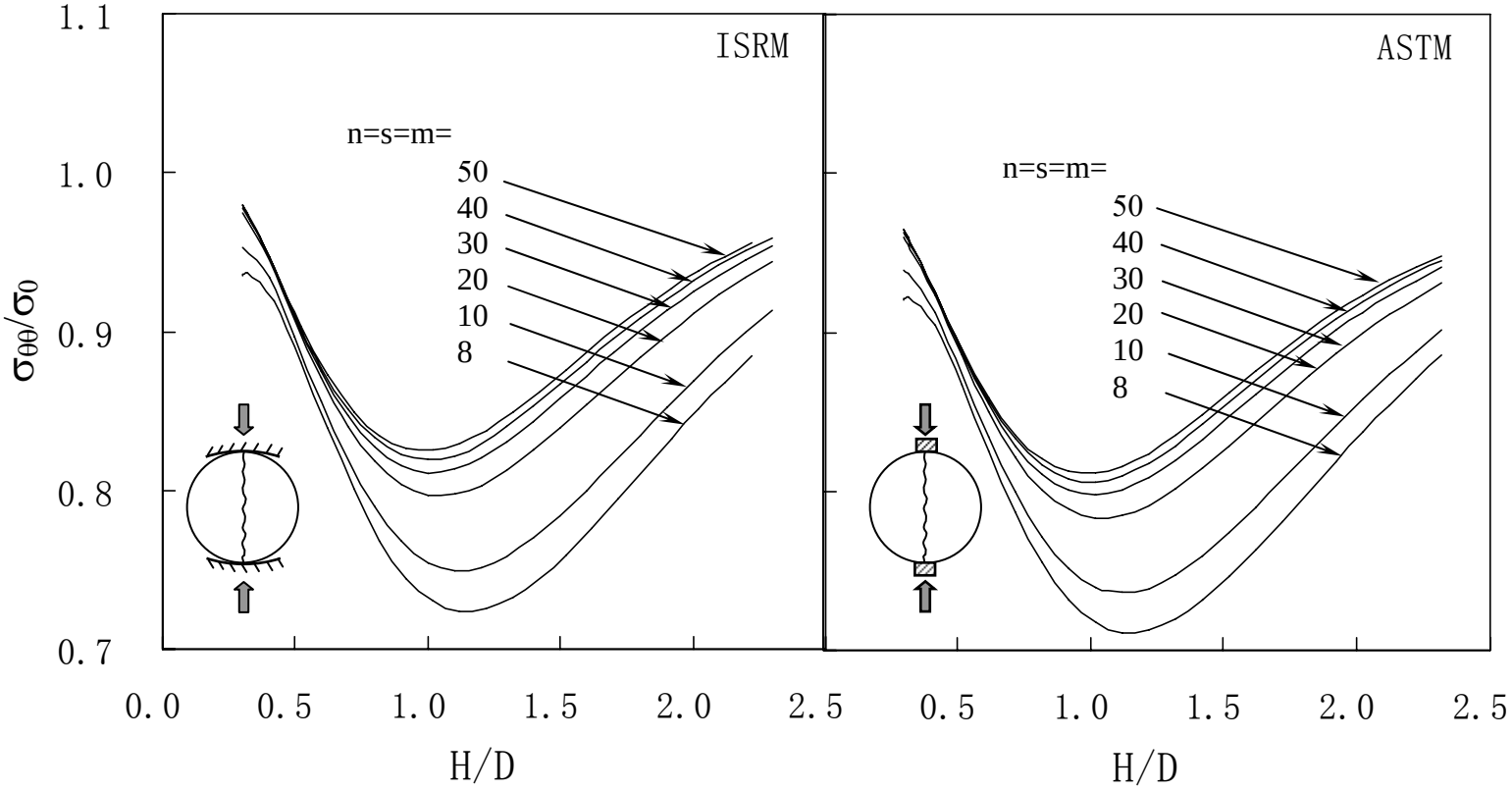

Fig. 4. The normalized hoop tensile stresses $\sigma_{\theta\theta}/\sigma_0$ at the center of the cylinder subjected to both ISRM and ASTM tests for various values of *n*, *s*, *m* and $\nu = 0.35$, where $\sigma_0 = 2F/(\pi D)$ is the 2-D Hertz solution. The line forces used in ISRM and ASTM tests are $F = 0.5MN/m$ and $F = 0.05MN/m$, respectively.

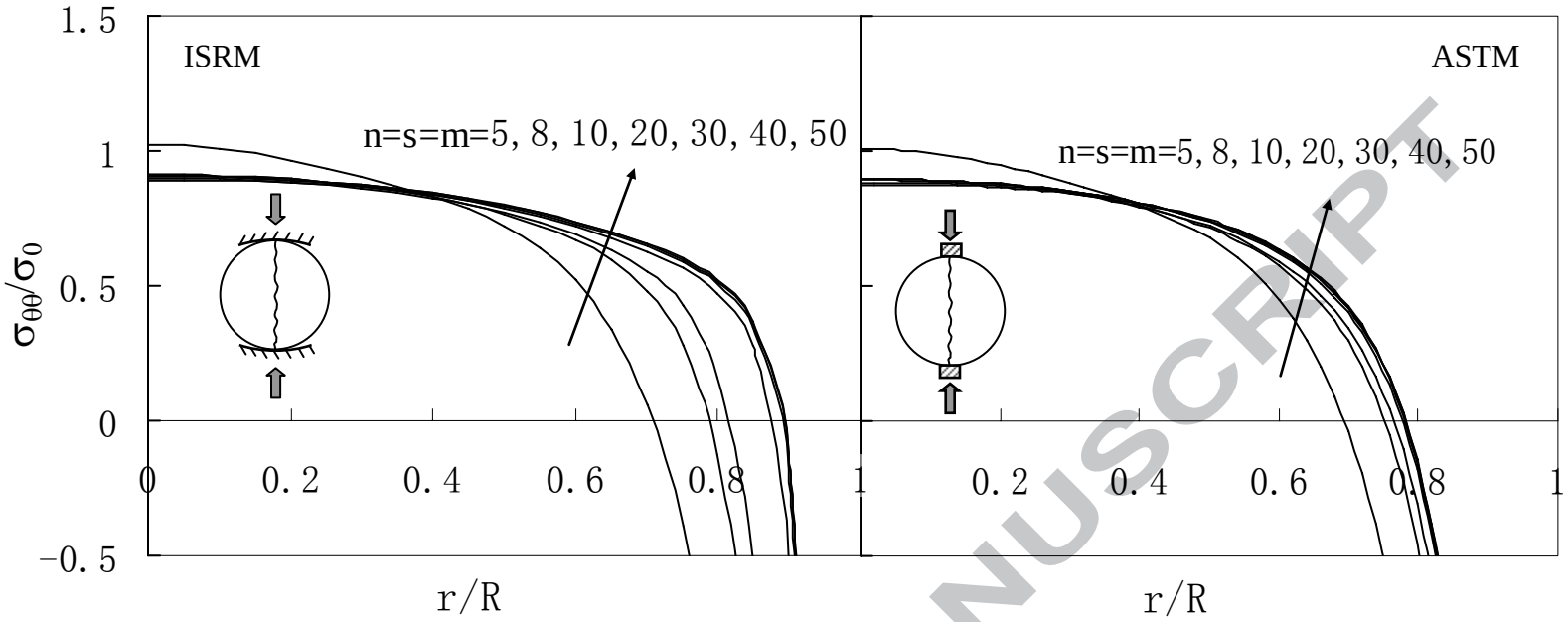

Fig. 5. The normalized hoop stresses $\sigma_{\theta\theta}/\sigma_0$ versus r/R for various values of n, s, m for $z/h = 0$, $\theta = 0$ and $\nu = 0.35$ for both ISRM and ASTM testing procedures. Other parameters used are the same as Fig. 4.

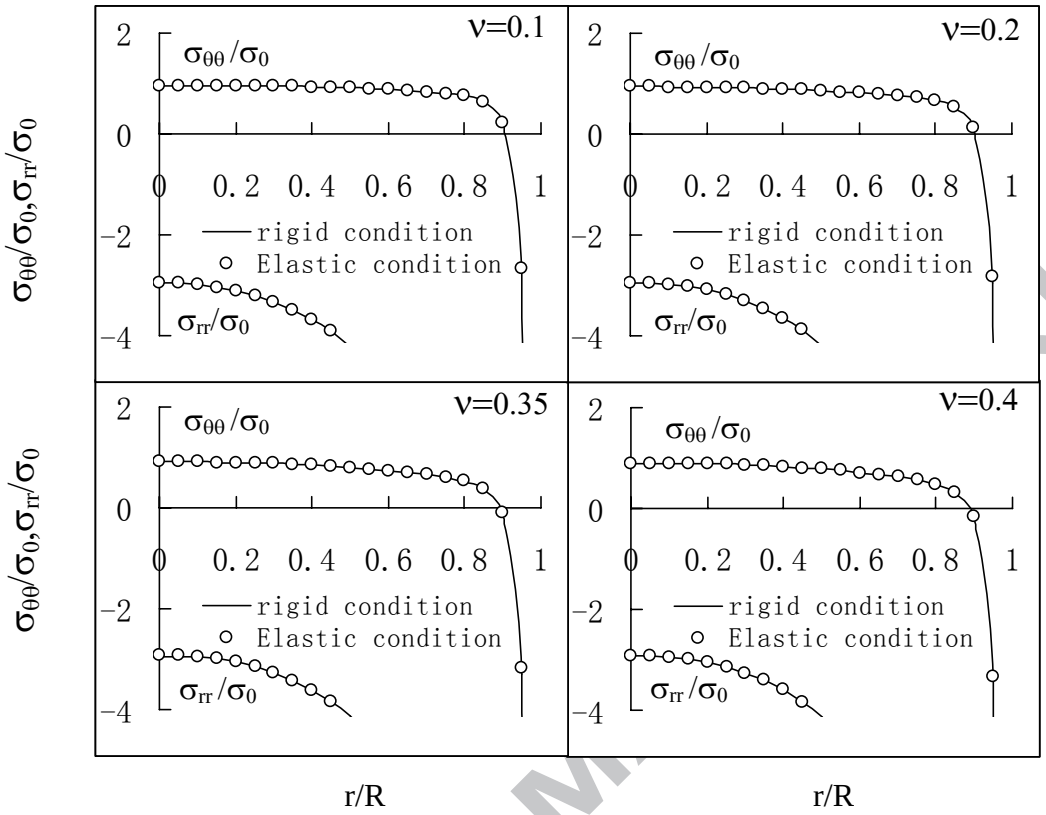

Fig. 6. The normalized stresses $\sigma_{\theta\theta}/\sigma_0$ and σ_{rr}/σ_0 versus the normalized distance *r/R* for *z/h* = 0, $\theta = 0$, and for various Poisson's ratio ν subjected to both rigid platen condition and elastic platen condition. The plots are for ISRM contacts and parameters used are: $E = 50\,GPa$, $D = 2R = 54$mm, $H = 0.5D$, $R_2 = -1.5$R. The Young's modulus $\bar{E}$ of the loading platen is assumed as 210 GPa whilst the Poisson's ratio being the same as those of the tested cylindrical material.

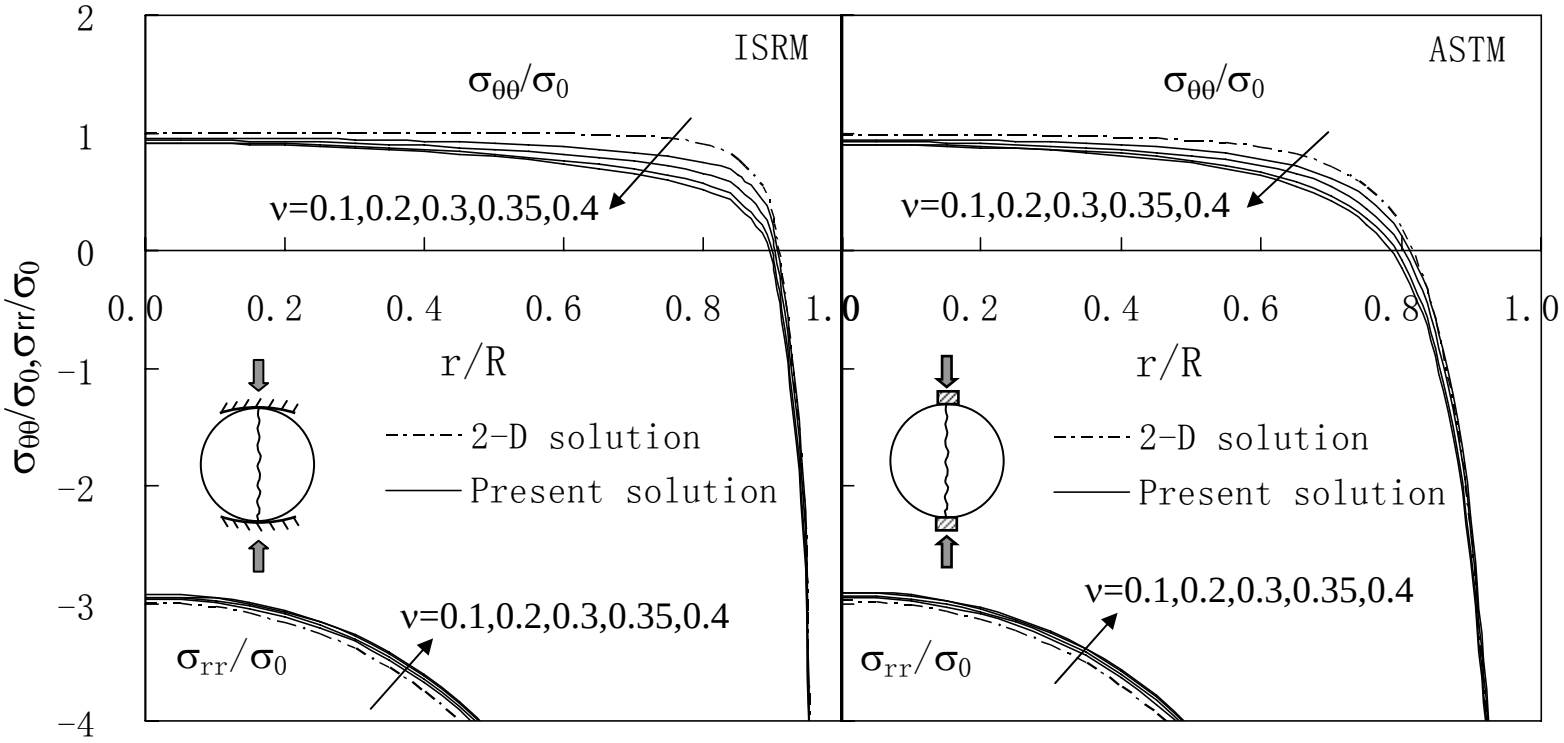

Fig. 7. The normalized radial and hoop stresses σ_{rr}/σ_0 and $\sigma_{\theta\theta}/\sigma_0$ versus the normalized distance *r/R* for *z/h* = 0, $\theta = 0$ and changing values of Poisson's ratio ν. The present 3-D solution and 2-D classical solution by Hondros (1959) are plotted as solid lines and center lines, respectively. Other parameters used are the same as Fig. 4.

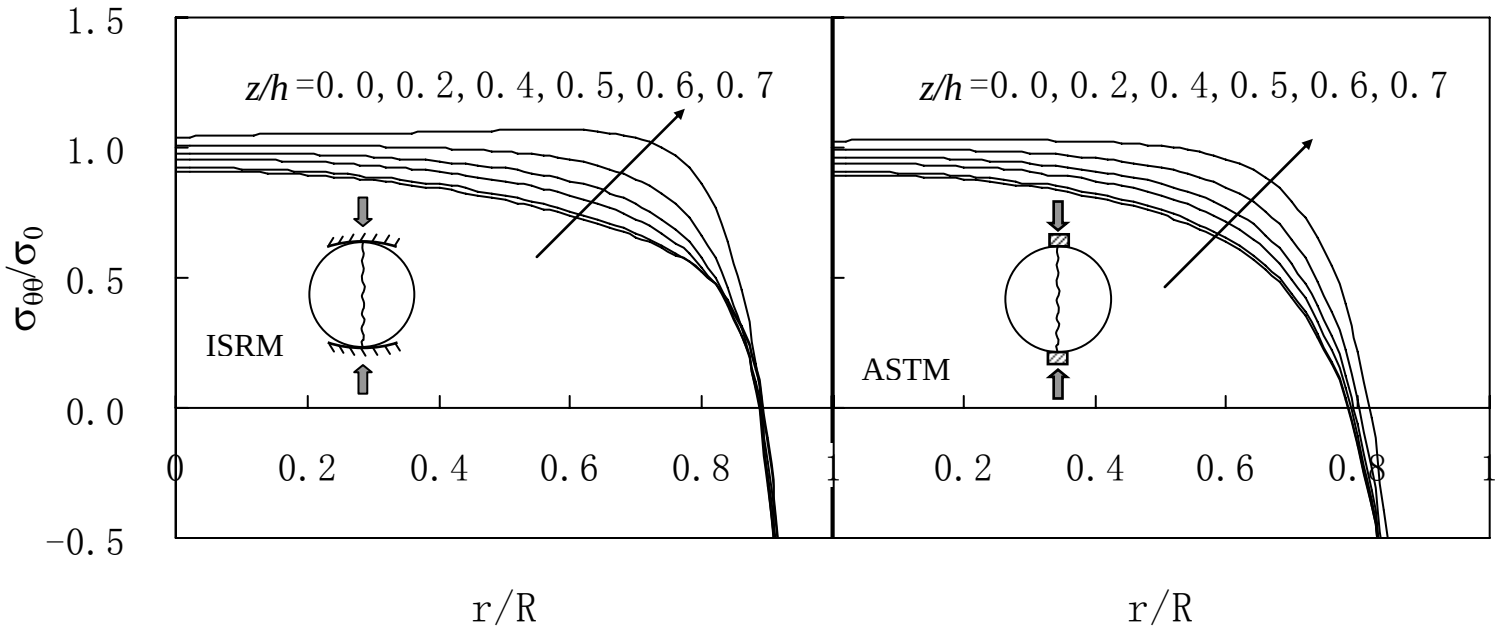

Fig. 8. The normalized hoop stress $\sigma_{\theta\theta}/\sigma_0$ versus *r/R* for various values of *z/h* for $\theta = 0$ and $\nu = 0.35$ for both ISRM and ASTM indirect tensile tests. Other parameters used are the same as Fig. 4.

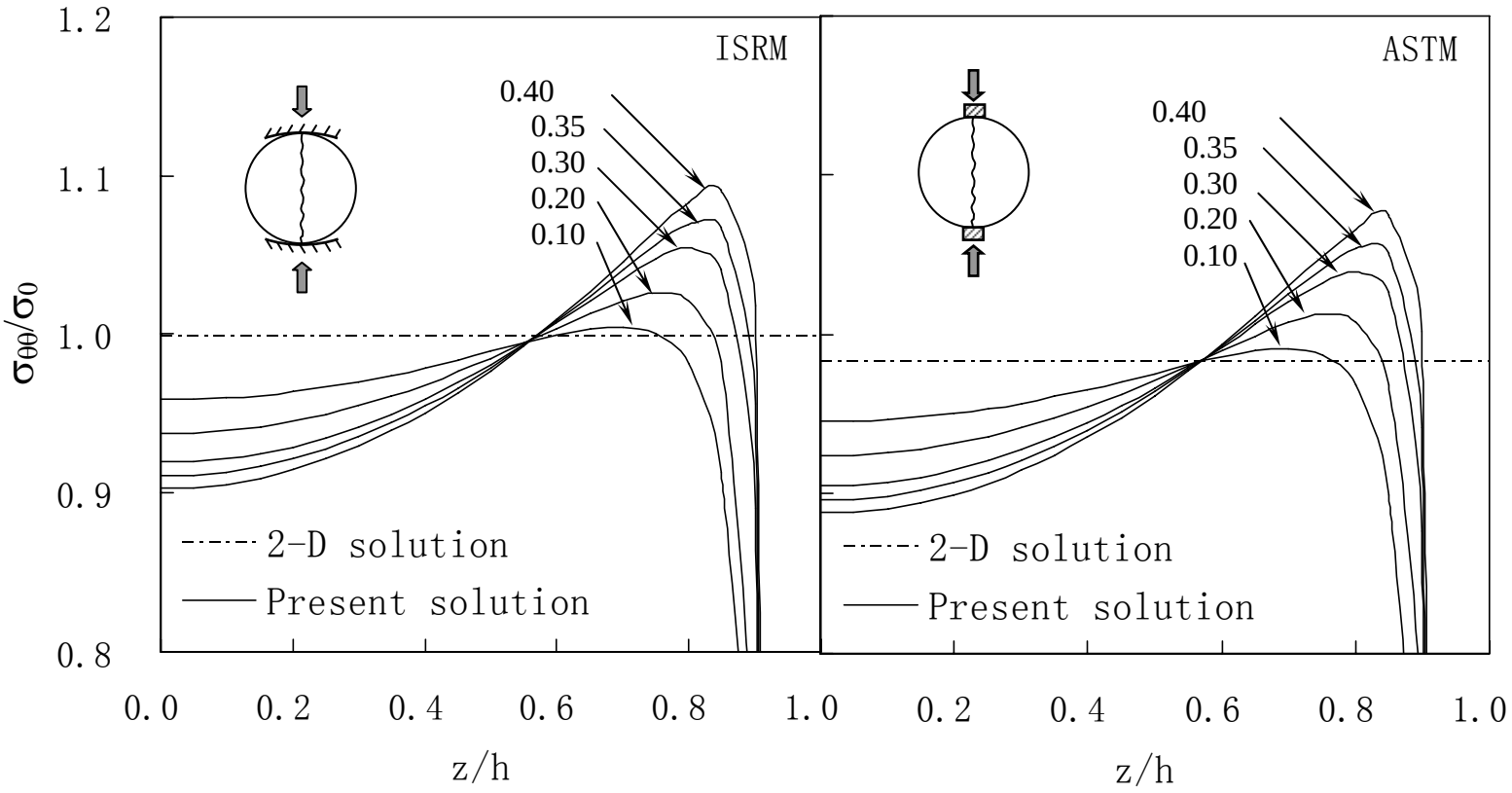

Fig. 9. The normalized hoop stress $\sigma_{\theta\theta}/\sigma_0$ versus the normalized distance *z/h* for *r/R* = 0, $\theta = 0$, and various Poisson's ratio ν. The 2-D Hondros (1959) solutions are also included as center lines.

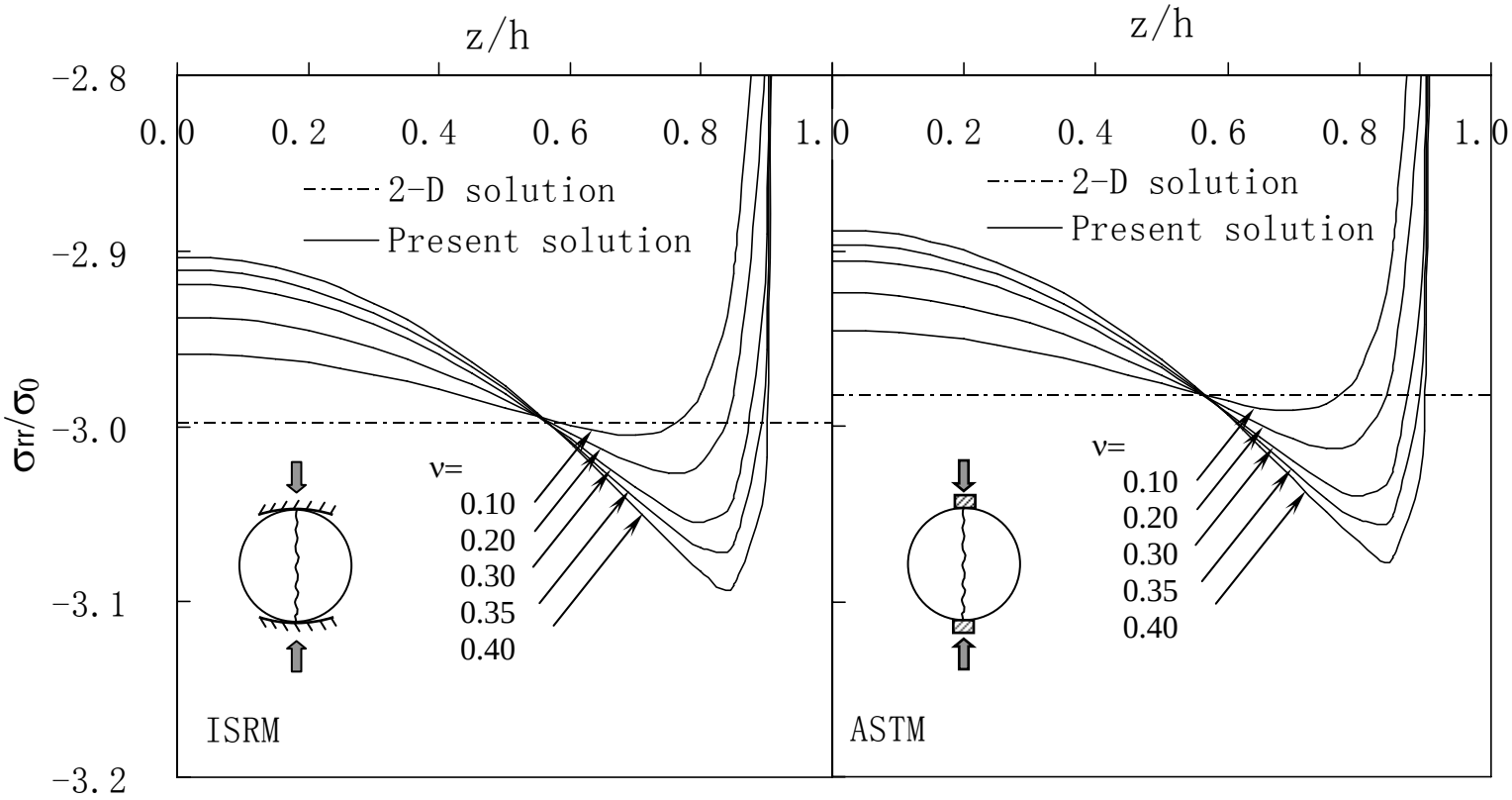

Fig. 10. The normalized radial stress σ_{rr}/σ_0 versus the normalized distance *z/h* for *r/R* = 0, $\theta = 0$, and various Poisson's ratio ν. The 2-D Hondros (1959) solutions are also included as center lines.

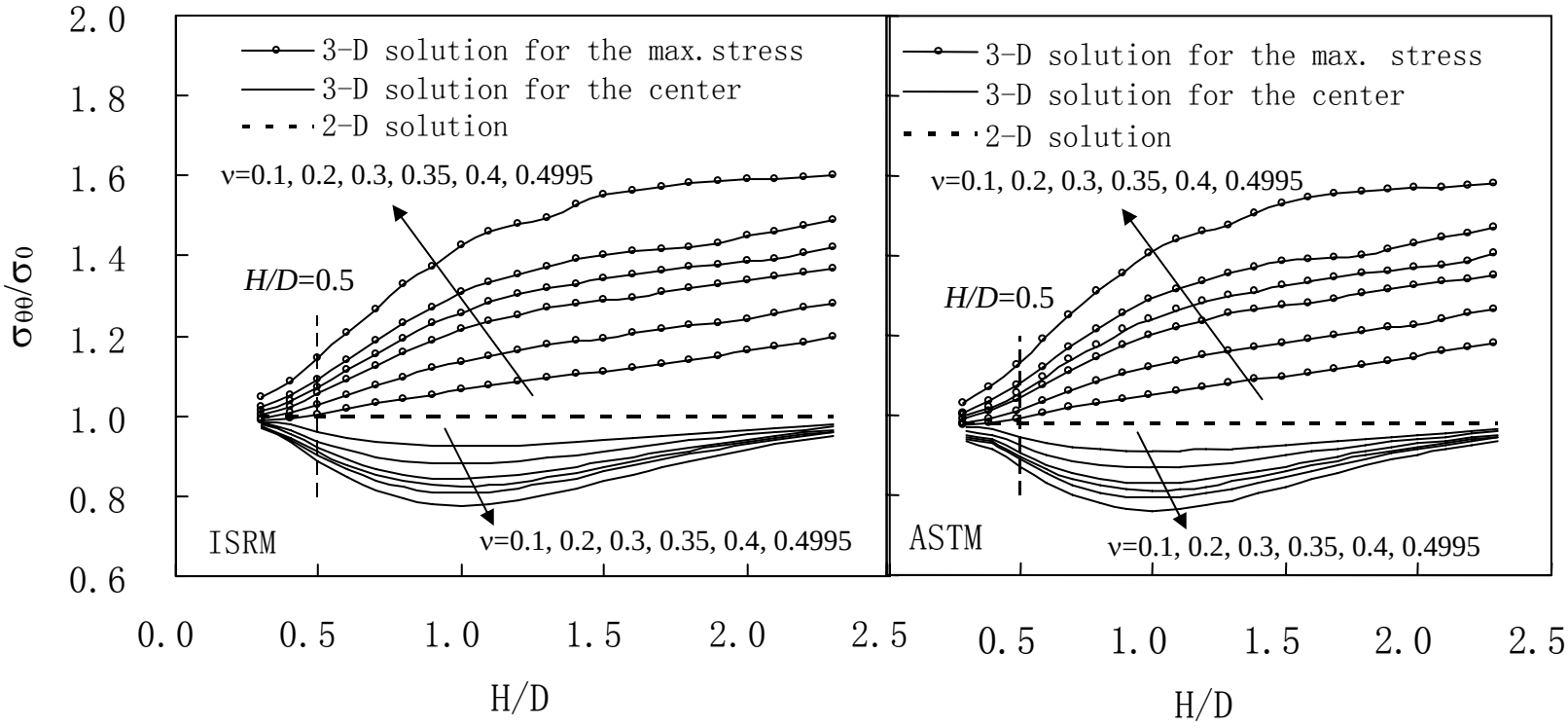

Fig. 11. The maximum normalized hoop stress $\sigma_{\theta\theta}/\sigma_0$ (solid lines with data points) and hoop stress at the center (solid lines) versus the height-to-diameter ratio *H/D* for various Poisson's ratio ν. The 2-D classical solution by Hondros (1959) are plotted as dotted lines.

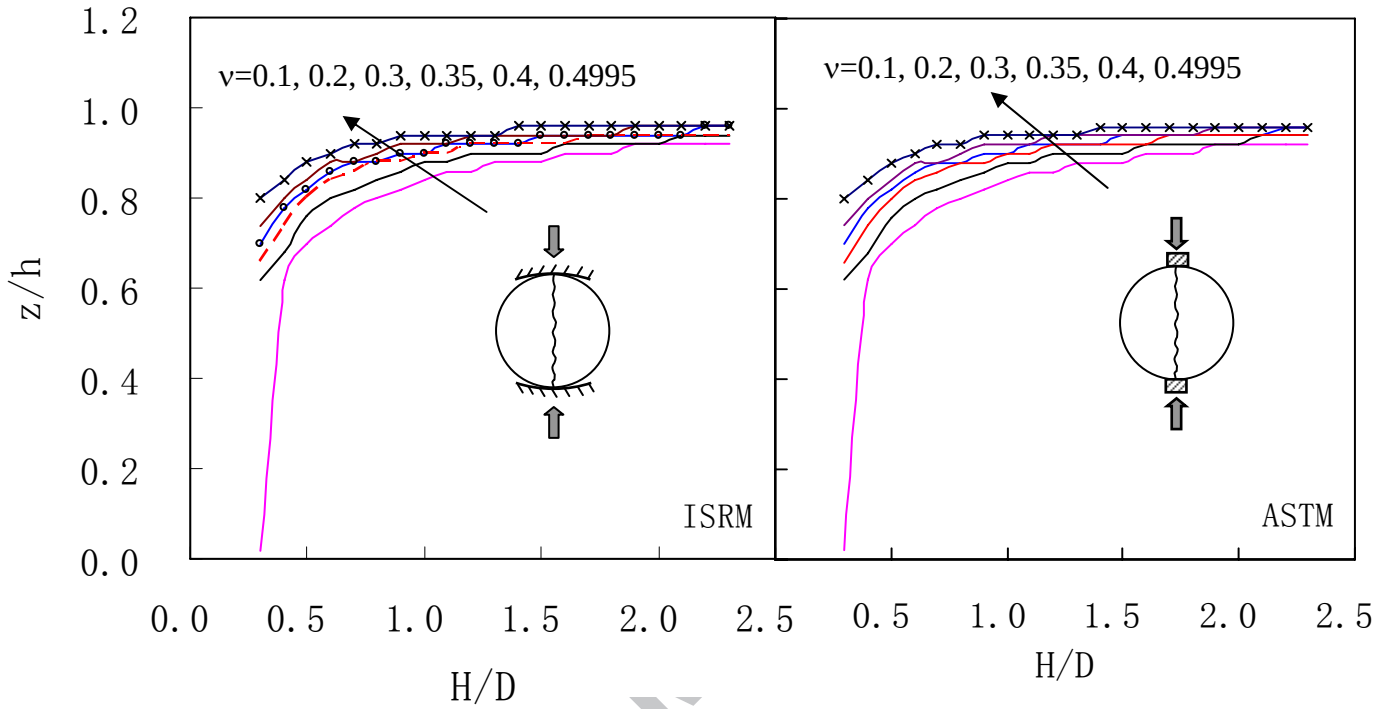

Fig. 12. The location *z/h* where the maximum tensile hoop stress is induced versus the height-to-diameter ratio *H/D* for various Poisson's ratio ν.

.